Modelled O2 airglow distributions in the Martian atmosphere

Marie-Ève Gagné, Stella Melo, Franck Lefèvre, Francisco González-Galindo, Kimberly Strong

Modeled O_2 airglow distributions in the Martian atmosphere

Marie-Ève Gagné,[1,2] Stella M. L. Melo,[1] Franck Lefèvre,[3] Francisco González-Galindo,[4] and Kimberly Strong[2]

Received 20 July 2011; revised 24 April 2012; accepted 25 April 2012; published 21 June 2012.

[1] We use a three-dimensional atmospheric model to study the airglow emissions from molecular oxygen in the Martian atmosphere. We estimate the O_2 Herzberg I & II, the Chamberlain, and the Infrared Atmospheric band emissions from different sets of kinetic parameters available in the literature. As expected, the enhanced production of atomic oxygen during daytime leads to stronger emissions at 12 hour local time than at 00 hour local time. Nevertheless, at night, the strongest emissions are found in the subtropics and around the terminator where the photochemistry of atomic oxygen is more active. Among the simulated emissions, we find that the Infrared Atmospheric emission is the most intense, as expected, and has maximum intensity reaching a few megarayleighs over the poles during the equinoctial seasons, and an average intensity over the equatorial latitudes of 50 kilorayleighs. We investigate the impact of different levels of water and dust content on airglow and we observe that the airglow structure is modulated by variations in the background atmospheric conditions. Moreover, comparisons of the emission with observations from instruments on board Mars orbiters and with ground-based measurements from Earth allow us to validate the consistency of our airglow model. Finally, we observe that the emission profiles from all band systems show structures; a double-layer profile is very frequent, and is representative of the vertical distribution of the current measurements of O_2 nightglow. This paper emphasizes the advantage of using three-dimensional global circulation models for the diagnostic of O_2 photochemistry in CO_2-dominated atmospheres.

Citation: Gagné, M.-È., S. M. L. Melo, F. Lefèvre, F. González-Galindo, and K. Strong (2012), Modeled O_2 airglow distributions in the Martian atmosphere, *J. Geophys. Res.*, *117*, E06005, doi:10.1029/2011JE003901.

1. Introduction

[2] The role of atomic oxygen in the photochemistry of the Martian atmosphere is undoubtedly important. In fact, the oxygen photochemistry controls the energetic budget in the 70 to 130 km altitude range, as revealed by model experiments [*Bougher et al.*, 1999; *González-Galindo et al.*, 2005; *McDunn et al.*, 2010]. Atomic oxygen is known to have an important effect on the CO_2 15-μm cooling. The collisions with atomic oxygen excite the vibrational states of the CO_2 molecules, enhancing the emission rate and thus the cooling. According to model simulations, changes in the atomic oxygen profile can produce variations up to a factor of 5 in the 15-μm cooling [*López-Puertas and López-Valverde*, 1995]. Given the uncertainty in the mechanisms that control the vertical distribution of atomic oxygen in the middle and upper atmosphere of Mars, the current Mars Global Circulation Models (GCMs) use a fixed atomic oxygen concentration in the calculations of the energetic balance [*Bertaux et al.*, 2006; *Forget et al.*, 2009; *González-Galindo et al.*, 2009; *McDunn et al.*, 2010]. Therefore, without proper validation of Mars Global Circulation Models (GCMs), an underestimation of the atomic oxygen content would yield an overestimation of the temperatures because of the role of CO_2 15-μm cooling in the thermal balance [*González-Galindo et al.*, 2005, 2009; *Huestis et al.*, 2008; *Forget et al.*, 2009; *McDunn et al.*, 2010].

[3] Remote sensing provides an attractive tool for measuring the atomic oxygen density in this altitude region. For Earth, airglow measurements provide a reliable method for determining atomic oxygen concentrations in the 50 to 120 km altitude range [*Sharp and McDade*, 1996; *She and Lowe*, 1998; *Melo et al.*, 2001]. Airglow refers to the emission of photons following radiative deactivation of electronically excited molecules in a planetary atmosphere. At night, the O_2 emissions arise from the recombination

[1]Space Science and Technology, Canadian Space Agency, Saint-Hubert, Québec, Canada.
[2]Department of Physics, University of Toronto, Toronto, Ontario, Canada.
[3]LATMOS, Université Pierre et Marie Curie, Paris, France.
[4]Instituto de Astrofísica de Andalucía, CSIC, Glorieta de la Astronomá, Granada, Spain.

Corresponding author: M. E. Gagné, Space Science and Technology, Canadian Space Agency, Saint-Hubert, QC J3Y 8Y9, Canada. (megagne@atmosp.physics.utoronto.ca)

0148-0227/12/2011JE003901

Table 1. Comparison of Measurements of O_2 1.27-μm Nightglow With OMEGA [*Bertaux et al.*, 2012] and SPICAM [*Fedorova et al.*, 2012] With Modeling Results[a]

Observations					Model	
instrument	L_S (°)	lat (°)	z_{max} (km)	I (MR)	z_{max} (km)	I (MR)
OMEGA	118	76.5 S	42	0.24	48	0.428
OMEGA	197	70 N	43.5	0.15	58	0.374
OMEGA	3	85 S	49	0.34	62	0.215
SPICAM	111	83.3 S	48–52	0.22	52	0.247
SPICAM	115	83.2 S	48–52	0.25	52	0.162
SPICAM	120	83.0 S	48–52	0.194	52	0.179
SPICAM	152	82.4 S	44–60	0.344	56	0.133
SPICAM	157	82.3 S	44–60	0.391	56	0.178
SPICAM	161	82.2 S	44–60	0.277	56	0.216
SPICAM	164	82.1 S	44–60	0.385	56	0.224

[a]The model results are given for the same latitude and season as for the observations.

reaction of oxygen atoms that were produced during daytime from photodissociation of CO_2, O_3, and O_2:

$$O(^3P) + O(^3P) + CO_2 \rightarrow O_2^\star + CO_2. \quad (1)$$

This three-body reaction involving two oxygen atoms in a CO_2 background produces O_2 in an excited state, denoted as $O_2^\star$, which can either emit a photon by radiative decay – reaction (2) – or be quenched by collision with another molecule, M_i, resulting in the loss of the excited state – reaction (3):

$$O_2^\star \rightarrow O_2 + h\nu \quad (2)$$

$$O_2^\star + M_i \rightarrow O_2 + M_i. \quad (3)$$

In the Mars atmosphere, the identity of M_i is most likely to be CO_2.

[4] The O_2 Infrared Atmospheric emission (herein referred as the O_2 IR or 1.27-μm emission) was first detected in the Mars dayglow from Earth by [*Noxon et al.*, 1976], and later observed by other Earth-based observatories [*Traub et al.*, 1979; *Novak et al.*, 2002; *Krasnopolsky and Bjoraker*, 2000; *Krasnopolsky*, 2003, 2007; *Farrel et al.*, 2005; *Novak et al.*, 2005]. The Spectroscopy for the Investigation of the Characteristics of the Atmosphere of Mars (SPICAM), an instrument on board the Mars Express orbiter, have been measuring the emission for the past few years [*Fedorova et al.*, 2006a, 2006b]. This spectral signature is the only recorded O_2 emission on Mars; the typical intensity of the 1.27-μm feature is about 1–30 MR [*Slanger et al.*, 2008]. Recently, the Observatoire pour la Minéralogie, l'Eau, les Glaces et l'Activité (OMEGA) instrument, also on Mars Express, observed for the first time the O_2 IR emission at nighttime [*Gondet et al.*, 2010; *Bertaux et al.*, 2011, 2012]. The feature was also measured by the Compact Reconnaissance Imaging Spectrometer for Mars (CRISM) on the Mars Reconnaissance Orbiter (MRO) around the same period [*McCleese and Kass*, 2010; *Clancy et al.*, 2011; R. T. Clancy et al., Extensive MRO CRISM observations of 1.27 μm O_2 Singlet Delta Airglow in Mars polar night and their comparison to MRO MCS temperature profiles and LMD GCM simulations, submitted to *Journal of Geophysical Research*, 2012]. And finally, *Fedorova et al.* [2012] reported measurements of the emission by SPICAM at nighttime. Table 1 summarizes the measurements of the O_2 IR emission observed in the Martian atmosphere at nighttime.

Table 2. Composition of the Venus and Mars Atmospheres

	Venus[a] (z = 95 km)	Mars[b] (z = 50 km)
T	150 K	180 K
CO_2	1×10^{15} cm^{-3}	8×10^{14} cm^{-3}
$O(^3P)$	2×10^{11} cm^{-3}	1.5×10^{11} cm^{-3}

[a]From VTGCM model [*Bougher et al.*, 2006].
[b]From LMD-MGCM model [*González-Galindo et al.*, 2009].

[5] Although not previously detected in the nighttime airglow of Mars, the O_2 visible emissions, comprising the Herzberg I, II, III and Chamberlain band systems, are expected to be present since they are observed on Venus [*Mullen et al.*, 2006; *Migliorini et al.*, 2011]. The similarity between the composition of the Venus and Mars atmospheres at the peak altitude for O_2 airglow (see Table 2) supports the assumptions that these emissions can occur in the Martian atmosphere but have yet to be detected. Possible explanations for the failure to detect O_2 visible emissions to date are the spectral sensitivity of previous instruments over the wavelength range of the emissions [*Krasnopolsky and Krysko*, 1976; *Migliorini et al.*, 2011], and the fact that the observations were mostly made during daytime when the spectral region is dominated by emissions from the strong Fox-Duffendack-Barker band system of CO_2^+ band systems [*Barth et al.*, 1971, 1972]. Table 3 gives the average intensity of the measured O_2 nightglow emissions in the planetary atmospheres of Earth, Venus, and Mars for comparison.

[6] In this paper, we simulate four O_2 airglow features in the Martian atmosphere at 00 and 12 hour local time (LT): the Herzberg I and II, and Chamberlain band systems that occur in the (UV) spectral region and spread into the visible part of the spectrum, and the IR emission. We use the atmospheric composition from a one-year simulation of the Laboratoire de Météorologie Dynamique (LMD) Mars GCM, commonly referred as the LMD-MGCM, using kinetic parameters derived from available laboratory measurements, and from Mars and Venus observations, we present our results for the expected magnitude range of these emissions on Mars. Our O_2 Herzberg and Chamberlain estimations represent, from the best of our knowledge, the first attempt to simulate these emissions for Mars using a 3-dimensional (3-D) model as inputs for atmospheric conditions. Using composition from a 3-D GCM provides the simulations with realistic dynamical variations projected onto the airglow features that cannot be studied with a

Table 3. Average Nighttime Emission Intensity of Selected O_2 Band Systems in the Planetary Atmospheres[a]

	Transition	Wavelength (nm)	Earth	Venus	Mars
Herzberg I	$A^3\Sigma_u^+ - X^3\Sigma_g^-$	240–440	500 R	140 R	
Herzberg II	$c^1\Sigma_u^- - X^3\Sigma_g^-$	260–450	120 R	5 kR	
Chamberlain	$A'^3\Delta_u - a^1\Delta_g$	320–480	200 R	700 R	
IR Atmospheric	$a^1\Delta_g, 0 - X^3\Sigma_g^-, 0$	1,270	100 kR	5 MR	280 kR

[a]See *Slanger et al.* [2008] and references therein.

simple 1-D photochemical model, which has been used in the past. Last, estimates for the daytime O_2 IR emission are compared to the observations from SPICAM, CRISM, OMEGA, and ground-based instruments on Earth as a means of checking the consistency of our airglow model.

[7] The data sets from the LMD-MGCM used in this study will be described in the next section, followed by a detailed explanation of our airglow model in section 3. In section 4, we discuss the specific mechanisms responsible for the production of each of the O_2 airglow emissions, as well as the results from the simulations of the emission profiles performed with different sets of parameters. The resulting vertically integrated intensity distributions are presented in section 5. Water and dust can change the atmospheric conditions; we take these into account and investigate how this would impact the airglow intensities in section 6.

2. Atmospheric Model

[8] The LMD-MGCM is a GCM for Mars that solves the primitive equations of hydrodynamics on a sphere by means of a grid point discretization. The first version of this model extended from the ground up to about 80 km above the surface, and included the radiative effects of CO_2 and suspended dust, a realistic CO_2 condensation scheme and a number of subgrid-scale processes [*Forget et al.*, 1999]. Parameterizations to account for the water cycle [*Montmessin et al.*, 2004] and for the photochemistry of the lower atmosphere [*Lefèvre et al.*, 2004] were later added to the model. The LMD-MGCM has been extended up to the thermosphere, so that its vertical range is now from the surface up to about 250 km. For that purpose, parameterizations to account for the physical processes important in this atmospheric region, such as the CO_2 radiative balance under non-LTE conditions, heating due to the absorption of UV solar radiation, molecular diffusion, the photochemistry of the rarefied upper atmosphere, and a number of other processes, have been included in the LMD-MGCM [*Angelats i Coll et al.*, 2005; *González-Galindo et al.*, 2005, 2009]. Although the photochemical scheme initially accounted only for species of the C, O and H families, it has been recently extended to include nitrogen chemistry [*González-Galindo et al.*, 2008].

[9] The calculations shown here have used as inputs the results of one Martian year simulation done with the LMD-MGCM including the photochemical packages described by *Lefèvre et al.* [2004] and *González-Galindo et al.* [2005], with updated kinetics data. The ozone columns calculated by the LMD-MGCM have been shown to be in good agreement with the ultraviolet measurements of SPICAM [*Lefèvre et al.*, 2008], which is important for our discussion of the emission initiated by the ozone photolysis. Model data have been provided on a 3-D grid with a resolution of 3.75° latitude × 5.6° longitude, on 50 vertical levels extending from the surface up to 150 or 250 km, depending on the version used. Results span the entire Martian year and have been extracted at 00 LT and 12 LT for each aerocentric longitude (L_S).

[10] In section 6 where the sensitivity of airglow to dust and water levels is discussed, we will refer to three different simulations performed with the LMD-MGCM, called "runs". The model run described in the previous paragraph will be referred as run 3, which run has been shown to represent satisfactorily the water distribution observed on Mars by the Thermal Emission Spectrometer on Mars Global Surveyor (MGS-TES) [*Lefèvre et al.*, 2008]. This means that the ozone distribution in the model also agrees with the ozone measurements [*Lefèvre et al.*, 2008], since the local amount of ozone on Mars is controlled by the abundance of odd hydrogen species produced by the photolysis of water vapor and its reaction with $O(^1D)$ [*Lefèvre et al.*, 2004]. For simulations run 1 and run 2, two different chemical schemes have been used: the *Lefèvre et al.* [2004] scheme for the lower layers (pressure larger than 1 Pa) and the *González-Galindo et al.* [2005] (extended to include N chemistry and ionosphere as in *González-Galindo et al.* [2008]) above this pressure level. Both photochemical models have been tested to provide similar results in the transition layer. While both simulations use a solar flux appropriate for solar average conditions, they differ in the dust load in the lower atmosphere: while for the first one a constant dust optical depth throughout the year is fixed, in the second one a variable optical depth as observed by TES during Martian Year (MY) 24 is used [*Clancy et al.*, 2000]. In summary, for run 1 the dust and water cycles have not been optimized, run 2 has a dust cycle matching MGS-TES MY24 measurements, but the same water cycle as run 1, and run 3 has the same dust cycle as run 2 and a water cycle matching the MGS-TES measurements.

3. Airglow Model

[11] In the atmosphere, relaxation of an excited state $O_2^\star$ to a less energetic excited state of O_2 from reactions (2) and (3) occurs multiple times before the excited state formed directly from reaction (1) loses all of its excess internal energy and reaches the O_2 ground state $X^3\Sigma_g^-$. The distribution of the excited O_2 population is therefore complex and it is difficult to differentiate between the direct yield of $O_2^\star$ from the three-body recombination and the total yield resulting from both the recombination, and the collisional and radiative relaxation processes. Here, we only consider the total yield for the excited state $O_2^\star$.

[12] The volume emission rate (VER) is described as the ratio of the production to the loss of the excited species, weighted by its lifetime. It represents the number of photons emitted per unit time per unit volume from radiative relaxation out of the $O_2^\star$ state into all lower states. The VER for the excited O_2 is expressed as follows:

$$\epsilon(O_2^\star) = \frac{[O_2^\star]}{\tau} \tag{4}$$

where τ is the lifetime by radiative relaxation of the specific excited state $O_2^\star$. At photochemical equilibrium, the concentration of $O_2^\star$ is the ratio between its production from reaction (1) and its loss from reactions (2) and (3):

$$[O_2^\star] = \frac{\alpha k_1 [O]^2 [CO_2]}{1/\tau + \sum_i k_{3i}[M_i]} \tag{5}$$

where α is the total yield of $O_2^\star$ and k_1 is the rate coefficient for the three-body recombination reaction (1), and k_{3i} is the quenching rate coefficient for the corresponding quenching species M_i in reaction (3).CO_2 and $O(^3P)$ are considered the

main quenching species and collisional removal by O_2, N_2, and CO is neglected. In this case, equation (4) becomes:

$$\epsilon(O_2^\star) = \frac{\alpha k_1 [O]^2 [CO_2]}{1 + \tau\left(k_{CO_2}[CO_2] + k_{O(^3P)}[O(^3P)]\right).} \quad (6)$$

Quenching coefficients of O_2 ($c^1\Sigma_u^-$) by N_2 and O_2 are of comparable magnitude, at least at high vibrational levels [*Copeland et al.*, 1996; *Slanger et al.*, 2007], but no measurements of the collision rate of this state with N_2 have been made at low vibrational levels. However, the measured quenching coefficients for N_2 and O_2 are an order of magnitude smaller than for CO_2 at $v' = 9$ [*Slanger et al.*, 2007]. Therefore, given the low abundance of N_2 (mixing ratio of 0.027) and O_2 (mixing ratio of 0.002) in the Mars atmosphere as compared to that of CO_2 (mixing ratio of 0.955), the quenching factors, i.e. $k_X[X]$, by N_2 and O_2 are negligible. While quenching of the state $c^1\Sigma_u^-$ by N_2 and O_2 is less effective than by CO_2, given their low abundance in the Mars atmosphere, *Slanger et al.* [2006] and *Slanger et al.* [2007] suggested that collisional removal by CO could be competing with that by CO_2. However, *García Muñoz et al.* [2009] concluded that CO is not the major quencher throughout the airglow layer given the fact that it barely changes the airglow profile in simulations where its quenching efficiency is given a weight equal to that of CO_2. *Krasnopolsky* [2011] also agrees that the branching ratio for the reaction with CO is minor in Mars and Venus. Therefore, we decided to neglect quenching by CO for the total quenching in our simulations.

[13] In this paper, we present the calculated VER with a fit to a Chapman distribution to illustrate some characteristics of the emission layer. The expression of the Chapman distribution follows the work of *Cox et al.* [2008, 2010] and *Royer et al.* [2010] to better capture the non-symmetry that is intrinsic to the loss and formation of the excited state:

$$\epsilon(O_2^\star) = \epsilon_{\max} \cdot \exp\left[1 - \frac{z - z_{\max}}{H} - \exp\left(-\frac{z - z_{\max}}{H}\right)\right] \quad (7)$$

where $\epsilon_{\max}$ is the maximum value of the VER in the profile, calculated in $cm^3\ s^{-1}$, $z_{\max}$ is the altitude in km at which this maximum occurs, and H is the e-folding depth in km of the emission layer, or characteristic width of the airglow layer that is, the distance over which the VER decreases by a factor of e as compared to its maximum value $\epsilon_{\max}$. The parameters we obtain from forcing our modeled VER to a fit with a Chapman function using a least squares fitting method, i.e. $\epsilon_{\max}$, $z_{\max}$, and H, along with the integrated intensity, I, allow quantitative comparisons with the available observations. The motivation for choosing this approach is based on two major arguments: first, this parameterization represents the balance between production and loss of $O_2^\star$; second, it provides a way to interpolate between the measured points, hence minimizing errors in the measurements as this interpolation is based on physical principles rather than mathematical. The limit of using a Chapman layer representation is that it does not capture dynamical features such as gravity waves. However, it is appropriate in this case since we are taking a climatological approach. The comparisons are made between modeled climate values and single-point observed profiles that are more susceptible to such events.

[14] The vertically integrated intensity from the ground to the top of the atmosphere (TOA) for each emission system is calculated in our model by:

$$I(O_2^\star) = \int_0^{TOA} \epsilon(O_2^\star) dz \approx \sum_i^{n_z} \epsilon(O_2^\star)_i \delta z_i \quad (8)$$

where n_z is the number of vertical levels in the model, $\epsilon(O_2^\star)_i$ is the VER at the altitude corresponding to the layer i and δz_i is the width of each vertical layer. In our airglow model, the integration is performed from 2 to 100 km.

[15] For the airglow simulations, the density profiles of $O(^3P)$, O_3, and CO_2 are given by the atmospheric model, as is the temperature profile (since the 3-body reaction rates used in our simulations are temperature-dependent). For each O_2 emission band system, we calculate vertically integrated intensity over the course of a year covering the whole latitudinal range. We also calculate the volume emission rate profile at specific locations and times: at latitudes 67.5°N, 0°, and 67.5°S for $L_S = 0°$, i.e. vernal equinox and 180°, i.e. autumnal equinox. The temperature and density profiles used in our calculations for these locations and seasons are shown in Figures 1 and 2 for 00 LT and 12 LT, respectively, for all three LMD-MGCM runs described in section 2. All simulations shown in this paper, except for the ones in section 6, were performed with the data set from run 3.

[16] For each emission band, the calculations are done using three different sets, called "cases", of kinetic parameters, namely different three-body recombination yields and rates, lifetimes, and quenching rates, for each band system. The kinetic parameters, i.e. α, k_1, τ, and k_{3i}, are taken from values reported in the literature and the details for each system will be given in the following section.

[17] Moreover, in section 6, we also show calculations at 12 LT for the O_2 IR emission using three different model inputs, namely runs 1 to 3 described in section 2. The goal of this exercise is to analyze the variations in airglow emission induced by different atmospheric conditions.

4. O_2 Volume Emission Rate

[18] The main path for excitation of electronically excited O_2 molecules during nighttime is the three-body recombination reaction (1) of atomic oxygen. Six bound electronic states of O_2 can be excited through this process: $a^1\Delta_g$, $b^1\Sigma_g^+$, $c^1\Sigma_u^-$, $A'^3\Delta_u$, $A^3\Sigma_u^+$, and $^5\prod_g$. These states were all first observed in the laboratory, except for the state O_2 ($^5\prod_g$), which was postulated from theoretical studies and later observed in Resonance Enhanced MultiPhoton Ionization (REMPI) spectra. The review of *Slanger and Copeland* [2003] is an excellent compilation of the laboratory and observational works related to these states. The O_2 electronically excited states are all metastable with respect to radiation and have lifetimes ranging from 0.16 s ($A^3\Sigma_u^+$) to 4500 s ($a^1\Delta_g$), allowing for collisions to occur before radiation [*Slanger and Copeland*, 2003]. Transitions between these states produce the emissions listed in Table 3.

[19] Although airglow has been studied for more than a century, the description of the physical chemistry producing the emissions remains a challenge [*Slanger and Copeland*, 2003]. For the Herzberg emissions, for example, there are still uncertainties regarding the rate coefficients for removal

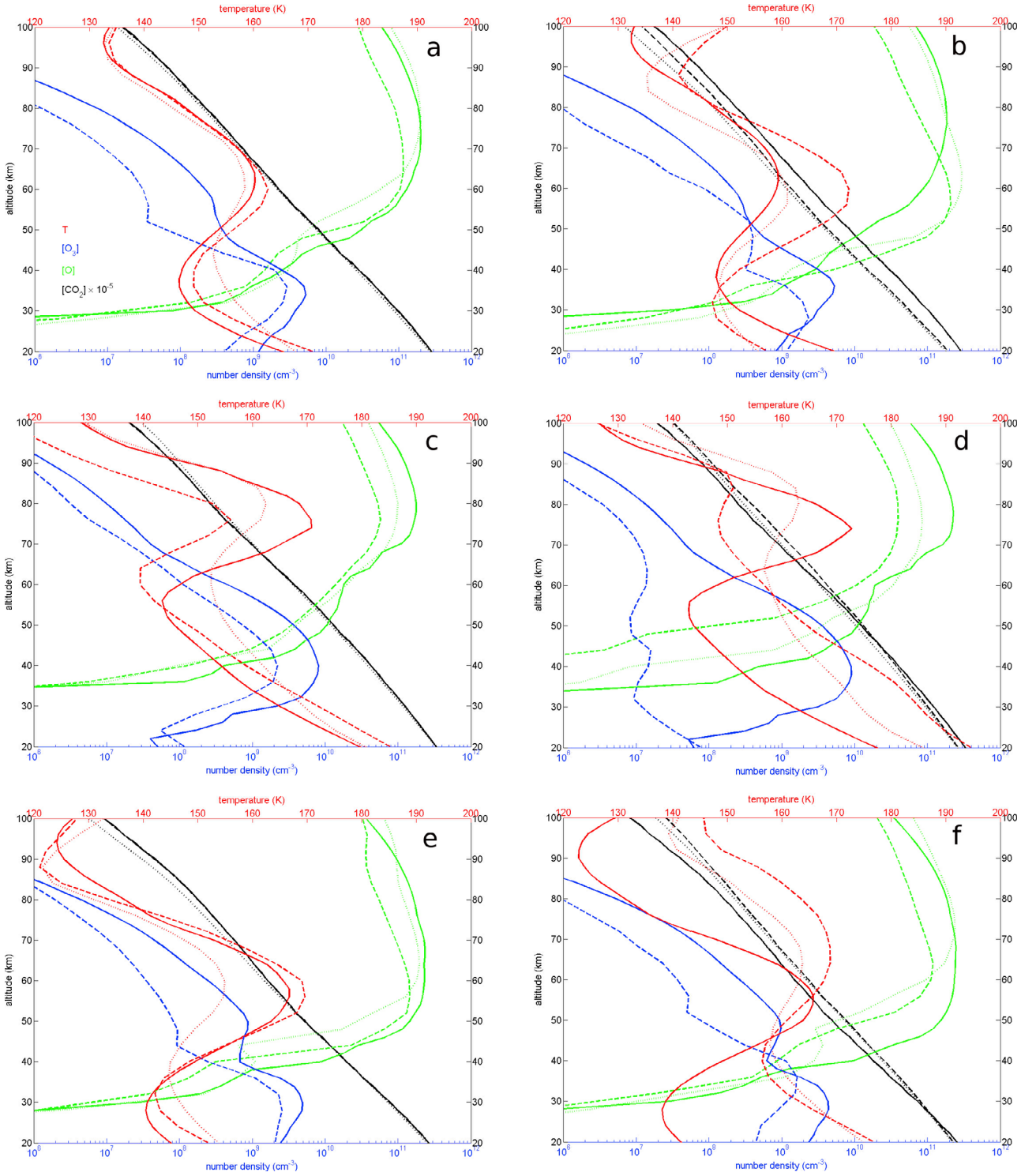

Figure 1. The 00 LT profiles of CO_2 (blue), O (green), and O_3 (magenta) density (cm^{-3}), and of temperature (K) (red) at (left) $L_S = 0°$ and (right) $L_S = 180°$ for latitudes (top) 67.5°N, (middle) 0°, and (bottom) 67.5°S. The dashed line corresponds to MGCM run 1, the dotted line is MGCM run 2, and MGCM run 3 is the solid line.

of $A^3\Sigma_u^+$, $A'^3\Delta_u$, and $c^1\Sigma_u^-$ by reaction (3), particularly in a CO_2 atmosphere. The rate coefficients previously measured in the laboratory in a flow discharge from the low vibrational levels [*Kenner and Ogryzlo*, 1980, 1983a, 1983b, 1984] are orders of magnitudes smaller than those recently measured at high vibrational levels using REMPI [*Knutsen et al.*, 1994; *Copeland*, 1994; *Copeland et al.*, 1996; *Hwang and Copeland*, 1997; *Mullen et al.*, 2006]. Furthermore, the complexity of the interplay between the metastable states of

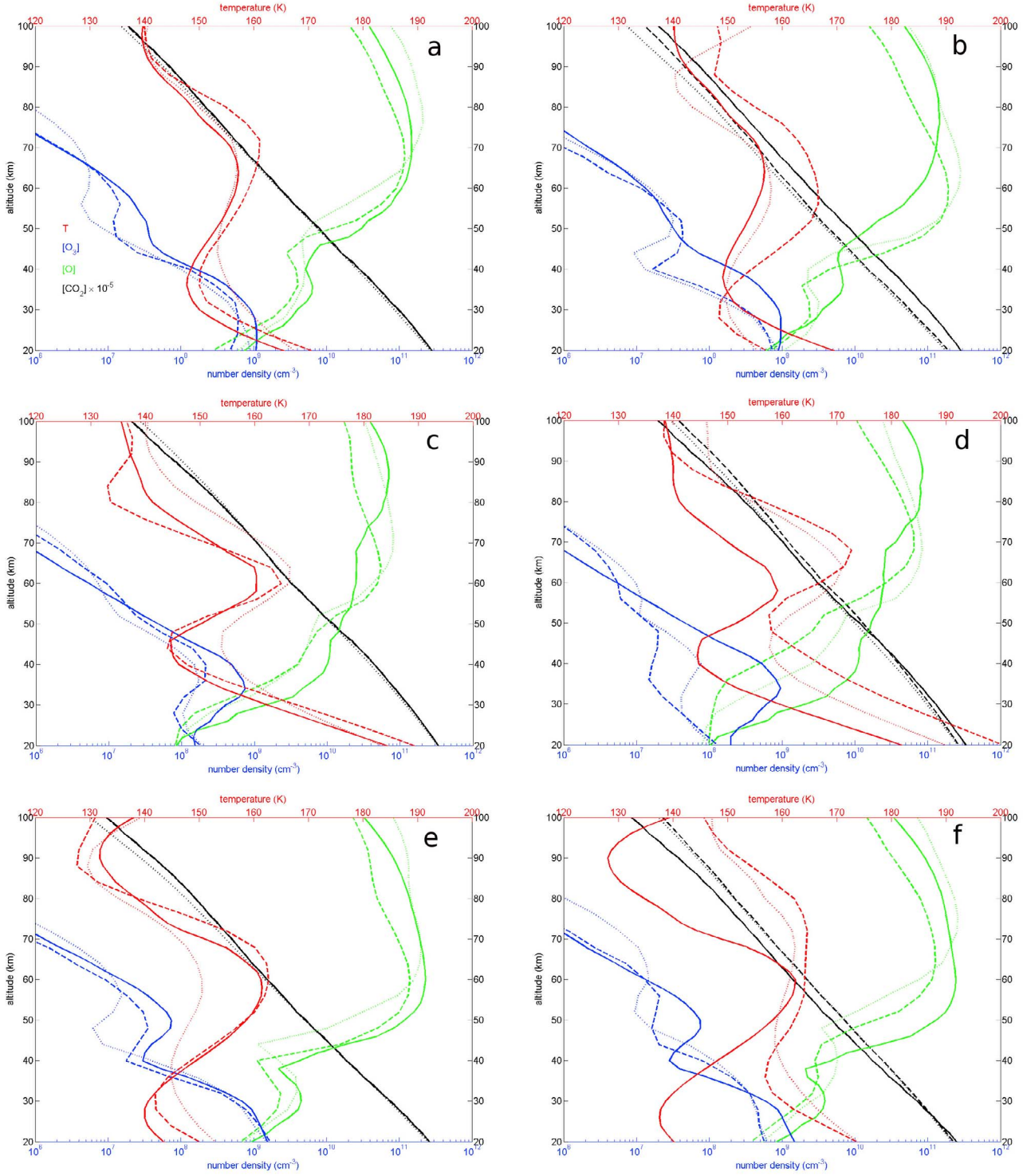

Figure 2. As in Figure 1 but for 12 LT.

O_2 is not fully understood, and this renders laboratory measurements of quenching rates even more difficult.

[20] A review by *Baulch et al.* [1976] shows that the absolute rate coefficient for the recombination of oxygen atoms is poorly determined, as is its dependence on temperature and on the nature of the third-body (see reaction (1)). Until recently, the coefficient from *Campbell and Thrush* [1967] was used by the combustion community, while atmospheric scientists adopted the value of *Campbell and Gray* [1973]. *Pejaković et al.* [2008] reported a new laboratory measurement of this rate coefficient, followed with a study by *Smith and Robertson* [2008] on its temperature dependence. These laboratory measurements were performed with N_2 as the third gas; it is generally accepted that the reaction with CO_2 would be 2.5 times larger following the proposition of *Nair et al.* [1994]. Recently, *Krasnopolsky*

Table 4. Kinetics Parameters Used in the Calculations of the VER of the Herzberg I Band

	Case 1	Case 2	Case 3
α	0.05[a]	0.06[b]	0.04[c]
k_1 ($cm^6\ s^{-1}$)	$2 \cdot 4.7 \times 10^{-33} \cdot (300/T)^{2}$ [d]	$2.5 \cdot 2.7 \times 10^{-33} \cdot (300/T)^{2}$ [e]	$2.5 \cdot 3 \times 10^{-33} \cdot (300/T)^{3.25}$ [f]
τ (s)	0.25[a]	0.16[g]	0.14[c]
k_{CO_2} ($cm^3\ s^{-1}$)	7×10^{-13} [h]	7×10^{-13} [h]	8×10^{-12} [c]
k_O ($cm^3\ s^{-1}$)	1.3×10^{-11} [i]	1.3×10^{-11} [i]	1.3×10^{-11} [i]

[a] *Krasnopolsky* [1986].
[b] *Bates* [1988].
[c] *Krasnopolsky* [2011].
[d] value of *Campbell and Gray* [1973] × 2 [*Krasnopolsky*, 1986].
[e] value of *Pejaković et al.* [2008] × 2.5 [*Nair et al.*, 1994].
[f] value of *Smith and Robertson* [2008] × 2.5 [*Nair et al.*, 1994].
[g] *Slanger and Copeland* [2003].
[h] *Kenner and Ogryzlo* [1983b].
[i] *Kenner and Ogryzlo* [1984].

[2009] suggested increasing the multiplicative factor of the rate coefficient of the recombination with CO_2 from 2.5 to 3.5, but then *Krasnopolsky* [2011] mentioned that this latter ratio could indeed be too high. *Jamieson et al.* [2009] measured a value for the recombination in presence of CO_2, as well as the yield of each excited states produced from this reaction. The value was measured at 200 K, and as expected, CO_2 is a more efficient third body than is N_2. To first degree, it seems appropriate to include the 2.5 multiplicative factor when using a rate coefficient measured with N_2 as the bath gas. In our simulations, we kept the rate used in each of the cited works for consistency with the kinetic parameters derived in these works.

4.1. Herzberg I Emission

[21] On Earth, the vibrational distribution of the $O_2(A^3\Sigma_u^+ - X^3\Sigma_g^-)$ emission band peaks at $v = 6$. Laboratory experiments where CO_2 was added to the atomic oxygen flow in an argon carrier produces a vibrational distribution shifted toward the lower levels, i.e., $v' = 0$–4 [*Stott and Thrush*, 1989; *Steadman and Thrush*, 1994]. The laboratory experiments of *Stott and Thrush* [1989], *Steadman and Thrush* [1994], and *Slanger and Copeland* [2003] show that vibrational relaxation is more important than quenching of the electronic state for the interaction of the O_2 ($A^3\Sigma_u^+$) state with CO_2. Cascading from $v = 7$ to $v = 6$ of $A^3\Sigma_u^+$ has been shown to be the dominant process with CO_2 as the quencher [*Slanger and Copeland*, 2003]. As mentioned above, *Stott and Thrush* [1989] concluded from their experiment that CO_2 causes collisional relaxation of $A^3\Sigma_u^+$ into the $c^1\Sigma_u^-$ state, which is also supported by the results of *Slanger and Copeland* [2003].

[22] Here, we assume that the three-body recombination reaction (1) populates the lowest levels of $O_2(A^3\Sigma_u^+)$. Our calculations were performed using equation (6); the kinetic parameters used in three different simulated scenarios are listed in Table 4. In case 1 of the Herzberg I simulations, we use the parameters derived empirically by *Krasnopolsky* [1986] following the Venus observations by Venera orbiters [*Krasnopolsky and Tomashova*, 1980], along with the quenching rate coefficients measured by *Kenner and Ogryzlo* [1983b, 1984] that are also used in the former reference. The second simulated case combines the kinetic parameters measured in the laboratory at low vibrational levels by *Kenner and Ogryzlo* [1983b, 1984] with the yield inferred by *Bates* [1988]. The last case for this emission is done with the best-fit set of parameters resulting from the model simulations of *Krasnopolsky* [2011] to match the Venus observations from the Venera era.

[23] Figure 3 shows the VER profiles for each simulated case at latitudes 67.5°N, 0°, and 67.5°S for $L_S = 0$ and 180°. Independently of the latitude and season, case 2 yields the strongest peak emission rate, with case 1 being slightly weaker. Case 3 is on average a factor of 1/3 to 1/4 the intensity of cases 1 and 2, respectively. The airglow layer peaks between 61 and 69 km over the polar regions, with case 3 peaking at a higher altitude than the other two cases, which is a consequence of stronger quenching by CO_2 in this latter case. The airglow layer has a mean topside scale height of 10 km. Over the equatorial regions, the VER profile exhibits a double-layer profile with the upper layer, at 85 km on average, being the most intense. This upper layer is thinner than the lower one, with a mean scale height of 6.5 km. The presence of this secondary peak is due to the maximum in O density that now occurs above 70 km. The temperature profile is also shifted upward by 10 km as compared to these in the polar regions (see Figure 1), and this directly increases the production of the excited state since, again, the recombination rates used here are temperature-dependent (see Table 4). The lower layer peaks at about the same altitude as the single-layer profile observed in the polar regions, that is near 65 km.

4.2. Herzberg II Emission

[24] According to the laboratory results of *Stott and Thrush* [1989] and *Steadman and Thrush* [1994], the population of the O_2 ($c^1\Sigma_u^-$, $v = 0$) state is greatly enhanced in the presence of CO_2. This is in agreement with the airglow observations on Venus, where the Herzberg II band is strong, unlike on Earth where the Herzberg II band is relatively weak (see Table 3). Following their Earth-based observations of the Venus spectrum, *Slanger et al.* [2007] proposed that in a CO_2 atmosphere, the $O_2(A^3\Sigma_u^+, A'^3\Delta_u)$ states are quenched down to the $O_2(c^1\Sigma_u^-\ v = 0)$ state by CO_2 and CO. *Steadman and Thrush* [1994] concluded from their experiments that collisional intersystem crossing of $A^3\Sigma_u^+$ and $A'^3\Delta_u$ cannot result in a vibrational distribution of the $c^1\Sigma_u^-$ state centered at the high vibrational levels. Therefore,

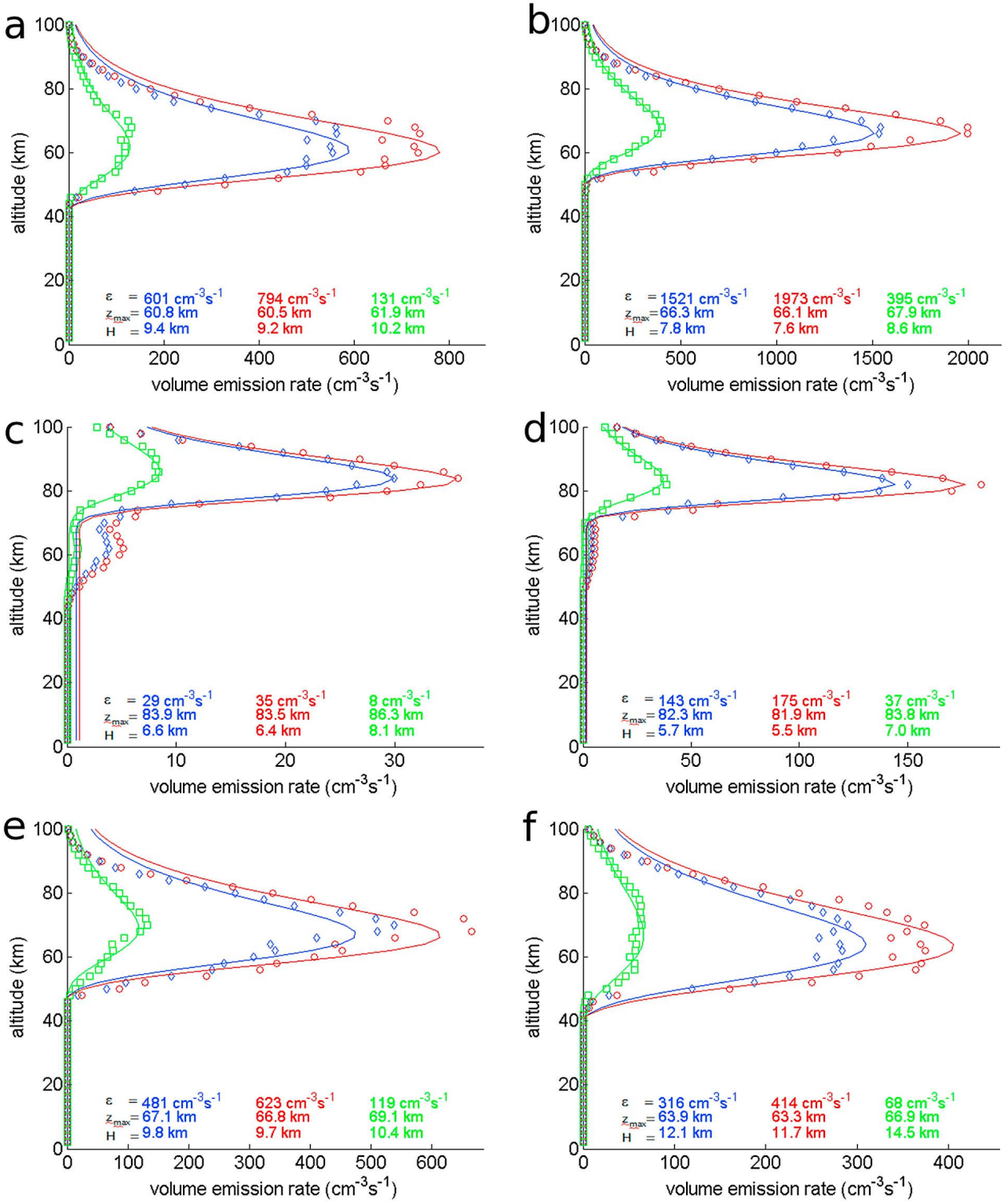

Figure 3. VER profiles for the O_2 Herzberg I emission at 00 LT at (left) $L_S = 0°$ and (right) $L_S = 180°$ for latitudes (top) 67.5°N, (middle) 0°, and (bottom) 67.5°S for three sets of kinetic parameters called "cases" (see text for details). Blue features are used for case 1, red for case 2, and green for case 3. The symbols are the calculated VER at each altitude from the airglow model, while the line corresponds to the Chapman layer fit for each VER profile; the fitting parameters, ϵ_{max} (Figure 3, top), z_{max} (Figure 3, middle), and H (Figure 3, bottom), are given.

Table 5. Kinetics Parameters Used in the Calculations of the VER of the Herzberg II Band

	Case 1	Case 2	Case 3
α	0.02[a]	0.04[b]	0.023[c]
k_1 ($cm^6\ s^{-1}$)	2.5×10^{-32} [d]	$2.5 \cdot 2.7 \times 10^{-33} \cdot (300/T)^2$ [e]	$2.5 \cdot 3 \times 10^{-33} \cdot (300/T)^{3.25}$ [f]
τ (s)	3.45[g]	3.7[h]	5–7[c]
k_{CO_2} ($cm^3\ s^{-1}$)	2.45×10^{-16} [a]	6×10^{-14} [i]	1.2×10^{-16} [c]
k_O ($cm^3\ s^{-1}$)	5.9×10^{-12} [i]	5.9×10^{-12} [i]	8×10^{-12} [c]

[a] *García Muñoz et al.* [2009].
[b] *Bates* [1988].
[c] *Krasnopolsky* [2011].
[d] *Slanger et al.* [2006].
[e] value of *Pejaković et al.* [2008] × 2.5 [*Nair et al.*, 1994].
[f] value of *Smith and Robertson* [2008] × 2.5 [*Nair et al.*, 1994].
[g] *Bates* [1989].
[h] *Huestis et al.* [1994].
[i] *Kenner and Ogryzlo* [1983a].

there should be a mechanism for collisional relaxation of the more energetic states, $A^3\Sigma_u^+$, $A'^3\Delta_u$, and $c^1\Sigma_u^-$ ($v > 0$), into O_2 ($c^1\Sigma_u^-$, $v = 0$) to explain the Venus airglow observations. Three possibilities have been proposed to explain this state population:

[25] 1. The three-body recombination with CO_2 as the third molecule is largely populating the $c^1\Sigma_u^-$ state [*Lawrence et al.*, 1977].

[26] 2. In the presence of CO_2, the quenching of $O_2(c^1\Sigma_u^-)$ would result in a vibrational cascade within the $c^1\Sigma_u^-$ state, hence enhancing the population of the $v = 0$ level [*Slanger and Copeland*, 2003].

[27] 3. The presence of CO_2 would quench the $A^3\Sigma_u^+$ and $A'^3\Delta_u$ states down to the $c^1\Sigma_u^-$ state, while O_2 and O quench the $A^3\Sigma_u^+$ and $A'^3\Delta_u$ states to lower electronic levels $O_2(X^3\Sigma_g^-, a^1\Delta_g, b^1\Sigma_g^+)$ [*Stott and Thrush*, 1989].

[28] Laboratory measurements favor options (2) and (3) to explain the enhanced population of the $c^1\Sigma_u^-$ ($v = 0$) state in the presence of CO_2. A plausible scenario would be a combination of collisional relaxation of the $A^3\Sigma_u^+$ (v) and $A'^3\Delta_u$ (v) states into the $c^1\Sigma_u^-$ state and vibrational cascading within the $c^1\Sigma_u^-$ state. Unfortunately, the contribution of each mechanism for the production of O_2 ($c^1\Sigma_u^-$) has not been entirely quantified. As mentioned in the discussion about the airglow model, we use a total yield for the production of the desired excited state to account for the different pathways for production of the excited states.

[29] We consider three scenarios for the production of the Herzberg II emission in a CO_2 atmosphere. Table 5 lists the kinetic parameters used to calculate the VER from this emission following each scenario and using equation (6); the results are shown in Figure 4. Case 1 is based on the recent observations of the Herzberg II transition by the VIRTIS instrument on Venus Express and the following analysis of the emission by *García Muñoz et al.* [2009]. The analysis from *García Muñoz et al.* [2009] resulted in a net production yield for the $O_2(c^1\Sigma_u^-, v = 0)$ state of 0.01–0.02 and a rate coefficient for quenching by CO_2 of 2.45×10^{-16} $cm^3\ s^{-1}$, when using the three-body recombination rate coefficient suggested by *Slanger et al.* [2006] and O quenching rate coefficient measured by *Kenner and Ogryzlo* [1983b]. For case 2, we also calculate the emission from the $c^1\Sigma_u^-$ state using the laboratory measurements of the removal rate coefficients at small vibrational levels by *Kenner and Ogryzlo* [1983a, 1984] along with the recombination yield of *Bates* [1988]. Case 3, uses the recommendations of *Krasnopolsky* [2011], which are a recombination yield of 0.023 and a removal rate coefficient by CO_2 of 1.2×10^{-16} $cm^3\ s^{-1}$. These latter values were derived from reanalysis of the measurements of this emission on Venus by Venera 9 and 10 [*Krasnopolsky and Tomashova*, 1980; *Krasnopolsky*, 1981, 1986].

[30] From Figure 4, we notice that case 3 always yields the largest peak emission rate (ϵ_{max}) and case 2 the smallest. The variations in the CO_2 removal rate in the simulated cases are responsible for this observed difference: the weaker the quenching of the excited state by CO_2, the larger is the scale height (H) and the higher is the maximum of the emission (z_{max}). The peak emissivity occurs between 51 and 66 km for all latitudes. The profiles at 0° latitude show a double-layer structure, as for the Herzberg I band emission, with the secondary peak around 80 km. However, the lower layer is now the strongest for most of the profiles. The difference in the quenching factor for this emission as compared to that for the Herzberg I is the reason for the predominance of the lower airglow layer observed here.

[31] Assuming that the processes responsible for the O_2 photochemistry in Venus and Mars atmospheres are coherent because of the similarity in the temperature, and CO_2 and atomic oxygen density profiles (see Table 2), we performed simulations for the same three cases using Venus nighttime conditions (not shown). After analysis of these simulations, we concluded that the set of parameters used in cases 1 and 3 better reproduce the expected ϵ_{max} and z_{max} observed on Venus. The difference in peak VER of the simulated profiles is one order of magnitude between these cases and case 2. Between cases 1 and 3, there is a factor of 2 difference in VER, which results directly from the difference in the quenching rates between the two cases. Moreover, case 3 tends to produce a peak emission at a lower altitude, i.e. lower z_{max}, then case 1, which is in better agreement with the observations from VIRTIS [*García Muñoz et al.*, 2009]. From the simulations presented here, we conclude that the quenching rate for the O_2 ($c^1\Sigma_u^-$) state by CO_2 should be revised to be about 2×10^{-16} $cm^3\ s^{-1}$. A low production yield of 0.02 seems to be reasonable to produce the emission intensity that would be expected on Mars, based on the above mentioned Venus simulations.

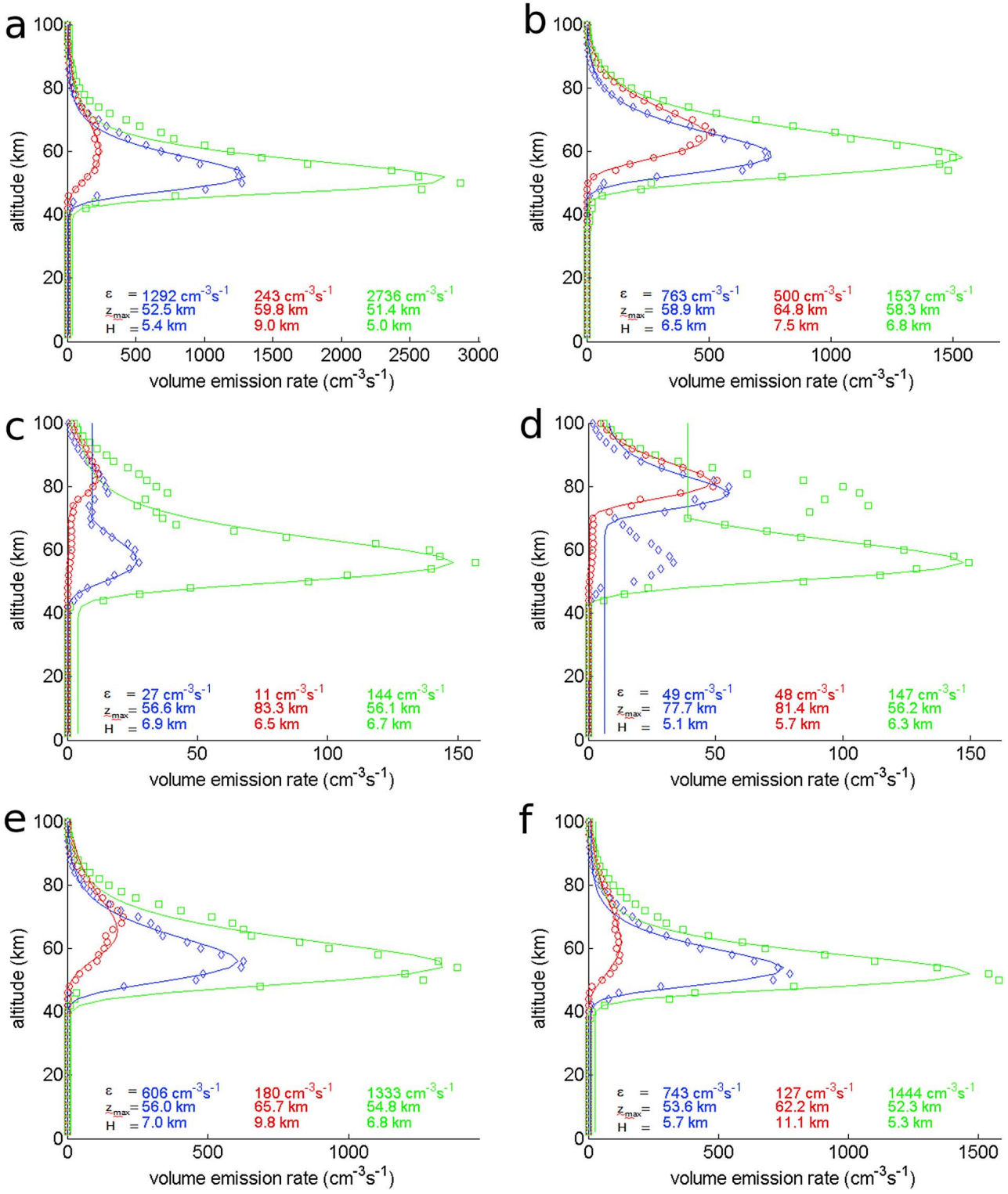

Figure 4. As in Figure 3 but for the O_2 Herzberg II emission.

4.3. Chamberlain Emission

[32] Many uncertainties remain for the production of the emission resulting from the $O_2(A'^3\Delta_u - a^1\Delta_g)$ transition. The proximity of the $A'^3\Delta_u$ electronic potential to that of $A^3\Sigma_u^+$ renders laboratory measurements of this state very difficult and hence, to our knowledge, not a single removal rate coefficient of $A'^3\Delta_u$ by any species has been measured in the laboratory yet. Therefore, it is challenging to make

Table 6. Kinetics Parameters Used in the Calculations of the VER of the IR Atmospheric Band

	Case 1	Case 2	Case 3
α	0.67[a]	0.5[b]	0.7[c]
k_1 (cm^6 s^{-1})	$1.2 \times 10^{-32} \cdot (300/T)^{2}$ [d]	2.5×10^{-32} [e]	$2.5 \cdot 3 \times 10^{-33} \cdot (300/T)^{3.25}$ [f]
τ (s)	4470[g]	4545[h]	4460[g]
k_{CO_2} (cm^3 s^{-1})	5×10^{-21} [c]	2×10^{-20} [i]	10^{-20} [j]
k_O (cm^3 s^{-1})		2×10^{-16} [i]	2×10^{-16} [i]

[a] *Krasnopolsky* [2003, 2006].
[b] *García Muñoz et al.* [2009].
[c] *Krasnopolsky* [2010].
[d] *Krasnopolsky* [1995].
[e] *Slanger et al.* [2006].
[f] value of *Smith and Robertson* [2008] × 2.5 [*Nair et al.*, 1994].
[g] *Lafferty et al.* [1998].
[h] *Newman et al.* [1999].
[i] *Sander et al.* [2006].
[j] *Krasnopolsky and Bjoraker* [2000].

any reasonable calculations for the VER profile of the Chamberlain transition.

[33] *Krasnopolsky* [2011] derived photochemical parameters for the production of the Chamberlain emission following assumptions based on observations of the band system. He used a production yield of 0.12 from theoretical calculations [*Wraight*, 1982; *Smith*, 1984], a three-body recombination rate of $3 \times 10^{-33} \cdot (300/T)^{3.25}$ cm^6 s^{-1} (scaled by a factor of 2.5) [*Smith and Robertson*, 2008], the same collisional removal rate by O as for the $A^3\Sigma_u^-$ state which is 1.3×10^{-11} cm^3 s^{-1} [*Kenner and Ogryzlo*, 1984], and derived a quenching rate by CO_2 of 4.5×10^{-13} cm^3 s^{-1} to fit the observations of the emission on Venus.

4.4. IR Atmospheric Emission

4.4.1. The 12 LT Profile

[34] To verify the internal consistency of our airglow model, we simulate emissions from the O_2 IR emission at 12 LT for comparison with the available observations. During the day, the photolysis of ozone is an additional source of oxygen in its excited state $a^1\Delta_g$:

$$O_3 + h\nu \rightarrow O_2(a^1\Delta_g) + O(^1D). \quad (9)$$

The contribution to the $a^1\Delta_g$ state formation from the three-body recombination reaction (1) is less important during daytime, but it is the major production mechanism at night. For the daytime simulations, we use a different expression for the calculations of the VER to include the production from O_3 photodissociation:

$$\epsilon(O_2^\star) = \frac{\beta J[O_3] + \alpha k_1 [O]^2 [CO_2]}{1 + \tau(k_{CO_2}[CO_2] + k_{O(^3P)}[O(^3P)])} \quad (10)$$

where J is the rate of photodissociation of O_3 and β is the yield of $a^1\Delta_g$ from this reaction. In our airglow simulations, we use the product βJ as calculated by the LMD-MGCM. The kinetics parameters for reaction (4) for each of the simulated cases of the IR Atmospheric airglow intensity are shown in Table 6. In brief, case 1 corresponds to the best-fit parameters derived by *Krasnopolsky* [2010] from Earth-based observations of the O_2 IR emission in the Venus atmosphere, while case 2 uses the parameters that best match the VIRTIS observations of Venus nightglow [*García Muñoz et al.*, 2009], and the laboratory parameters for production and loss of $a^1\Delta_g$ make case 3, as this set is also used in the analysis of *Krasnopolsky* [2011] to reconcile the observations of the emission on both Earth and Venus.

[35] The VER profiles calculated for the three different cases at several latitudes and seasons are shown in Figure 5. The daytime airglow emissions mimic the ozone concentration throughout the vertical range, as can be seen in Figure 2, since it originates mainly from the production of the $a^1\Delta_g$ state through photodissociation of ozone. The contribution from O-O recombination is then negligible. The profiles all have a double layer structure, except for $L_S = 0°$ at latitude 0° (see Figure 5c). The lower layer is mainly due to $O_2(a^1\Delta_g)$ that is quenched at larger pressures, combined with the emission rate decreasing with increasing height. Contrary to the 00 LT profiles previously discussed for the other transitions, the layer close to the ground is the more intense during the day and has itself a double peak, although not properly defined. Over the equator, the double-peak feature of the lower airglow layer is better defined. Over the poles, the emission rate within this lower layer reaches a maximum below 30 km, then decreases with decreasing altitude, and increases again down to the surface. At these latitudes, the availability of O_3 results in an emission at 1.27 μm down to the surface, even in the presence of quenching. The uppermost layer peaks between 50 and 60 km in the polar regions, while the peak VER of the upper layer is shifted upward by about 10 km over the equator.

4.4.2. The 00 LT Profile

[36] We now present predictions for the nighttime O_2 1.27-μm emission following our airglow simulations. During the night, the main production mechanism for O_2 ($a^1\Delta_g$) is shut down, i.e. reaction (9) is no longer active, so that the intensity is greatly reduced, except during the polar night, when the VER is increased by two orders of magnitude as compared to that over the equatorial regions. The increase in O_2 emission above the winter poles is due to downward transport of large amounts of O produced in the thermosphere [*Gondet et al.*, 2010; *Bertaux et al.*, 2011, 2012; *Clancy et al.*, 2011; Clancy et al., submitted, 2012].

[37] The VER profiles at 00 LT for this emission are more homogeneous from case to case as compared to the other

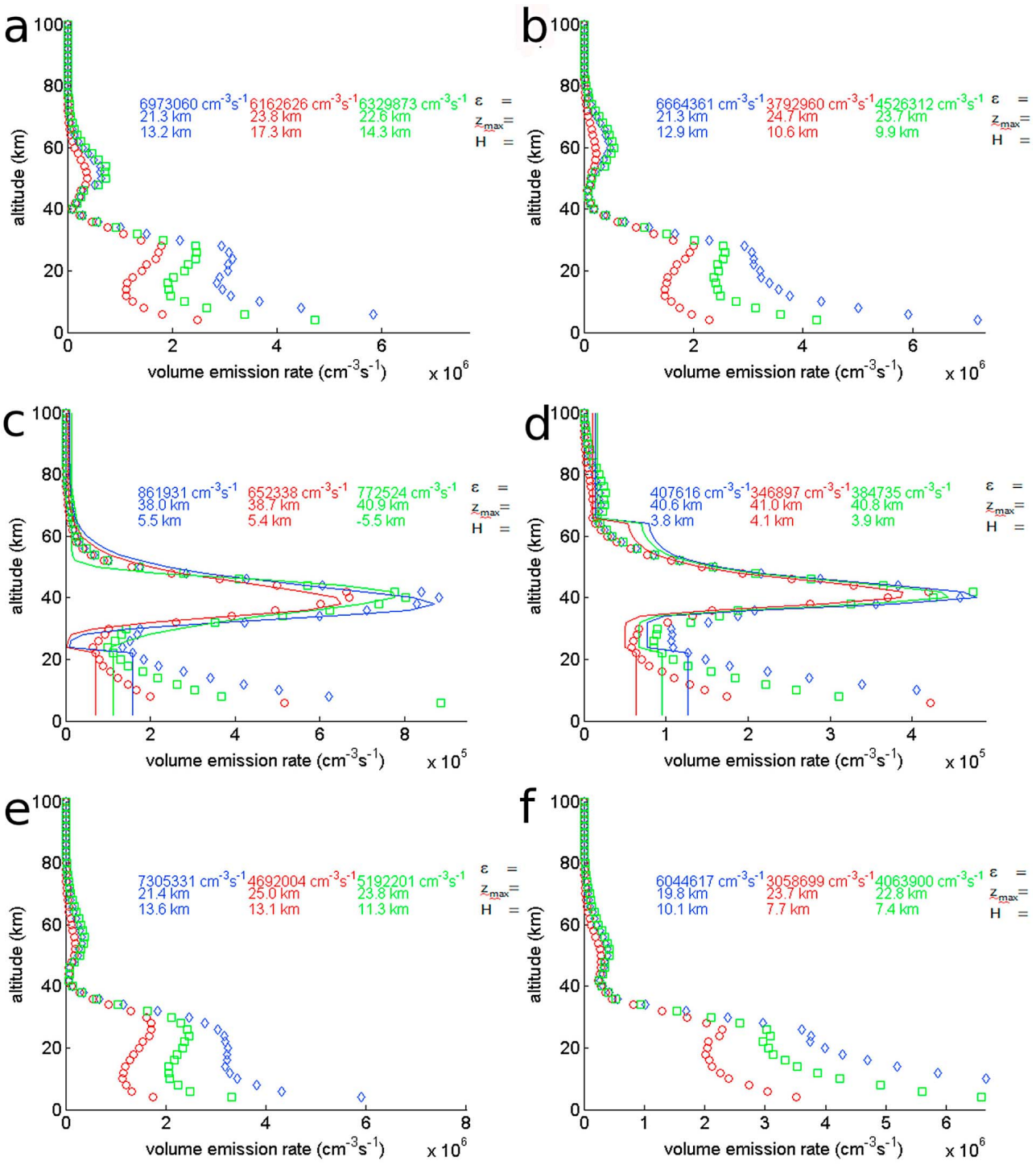

Figure 5. As in Figure 3 but for the O_2 IR Atmospheric emission at 12 LT.

band emissions as can be seen in Figure 6. The peak VER changes mostly in response to the production yield, with case 3 being the strongest and case 2 the weakest. The peak altitude, which is mostly determined from the collisional removal rate, is constant among the simulated cases for a given atmospheric background and varies between 53 and 61 km in the polar regions depending on the season. The scale height shows minimal variations across the simulations; the mean is 6 km with a standard deviation of 1 km.

[38] Observations of O_2 nightglow emissions from CRISM show that the peak altitude is within the 46–56 km altitude region for latitudes above 70°S and for the period L_S = 50–137° [*Clancy et al.*, 2011; Clancy et al., submitted, 2012]. Most profiles show a double-peaked vertical

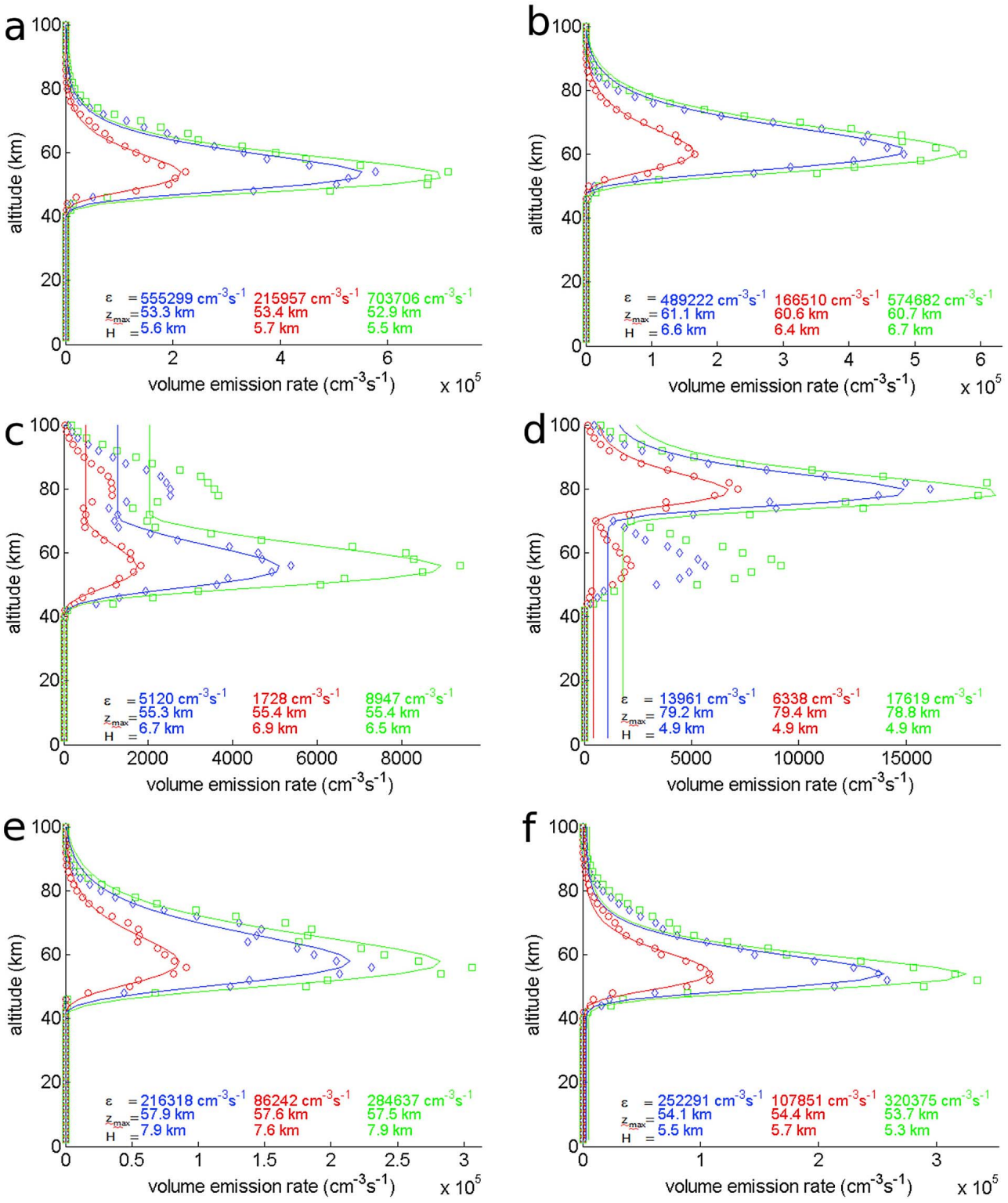

Figure 6. As in Figure 3 but for the O_2 IR Atmospheric emission at 00 LT.

structure, with the highest peak around 57 km and the lower peak near 50 km. Moreover, the measurements show a large diurnal variability in the emission rate with values at the peak differing by a factor of 2. We note that these results are preliminary and an in-depth comparison will only be possible when more results will be published.

[39] In our simulations, the profiles at the equator show a double peak feature with the upper layer being weaker than

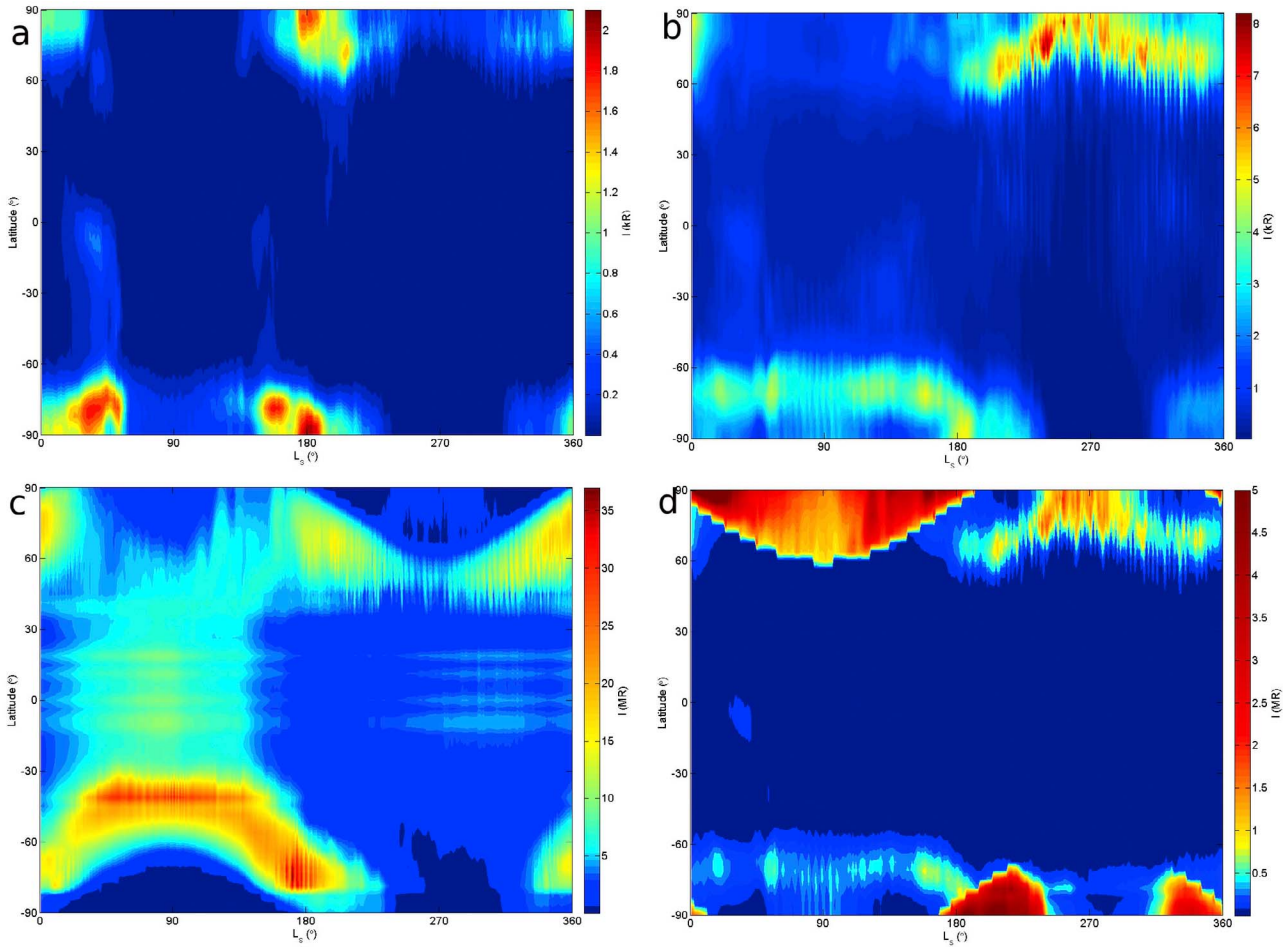

Figure 7. Global distribution of intensity of the O_2 emission bands for the (a) Herzberg I emission; (b) Herzberg II emission; (c) IR Atmospheric emission at 12 LT; and (d) IR Atmospheric emission at 00 LT (see text for details). The color bar is the intensity in R for the upper panel and in MR for the lower panel.

the lower one for $L_S = 0°$ while the upper layer is the most intense at $L_S = 180°$. The uppermost layer peaks at 80 km and the lower one reaches its maximum near 55 km. The vertical distribution of this emission is very similar to that for the Herzberg II emission, with peak VER located at about the same altitudes for these two transitions, while the profiles for the Herzberg I band peak at higher altitudes.

5. O_2 Vertically Integrated Intensity

5.1. Herzberg I

[40] The Herzberg I system has not been observed in the atmosphere of Mars but a detection of the emission in the Venus atmosphere was reported by *Krasnopolsky and Tomashova* [1980]. The total intensity reported for this band is 140 R and the observed spectra show emission out of the $v' = 0$ level. The spectra were recorded between 19 and 05 LT and latitudes of ±30°. To our knowledge, the detection of this band in a CO_2 atmosphere has never been repeated, which limits the extent of the comparison with our calculations.

[41] According to our simulations, the maximum intensity reaches above 2 kR in case 3 over the polar regions and the maxima are localized shortly before/after the vernal/autumnal equinoxes. Over the equator, the maximum intensity drops by one to two orders of magnitude due mainly to the larger production of the excited state resulting from a larger atomic oxygen mixing ratio between 50 and 70 km in the polar regions. As for cases 1 and 2, the intensity range is larger by a factor of 3 to 4, respectively, as compared to simulated case 3. However, the structure of the annual distribution is similar, with a bimodal maximum in the polar regions during the polar nights. Figure 7a gives a representation of the global distribution of the emission following the case 3 scenario.

[42] From the discussion of *Krasnopolsky* [1986], the observed Venus intensity for the Herzberg I transition is 140 R and the calculations reported in that study yield an expected intensity of 2 R for Mars, resulting in a Venus-to-Mars intensity ratio of 70. Case 3 of our simulations is the one that yields the lowest intensity values, with values as low as a few rayleighs up to around 200 R over the

equatorial region. This simulation gives a maximum intensity of about 2 kR during the Southern Hemisphere polar night and slightly lower values for the Northern Hemisphere. The intensity range for cases 1 and 2 is typically an order of magnitude greater than for case 3. This latter case seems to be in better agreement with the expected intensity of *Krasnopolsky* [1986] and *Krasnopolsky* [2011]. Therefore, it is our suggestion that the removal rate coefficient of the $A^3\Sigma_u^+$ state for quenching by CO_2 should be revised to account for greater loss of this excited state through this pathway. *Slanger and Copeland* [2003] also favor increasing the rate coefficient of *Kenner and Ogryzlo* [1983b, pp. 209–212] by one order of magnitude with the argument that "the trends of the higher levels suggests that [the latter] afterglow results underestimate the magnitude of the removal rate coefficients, a conclusion previously reached by aeronomic modelers."

[43] We continue by exploring the relationship between the Herzberg I and Herberg II (further discussed below) emissions, to preserve the consistency between Mars and Venus observations. If we apply the Venus-to-Mars ratio of intensity suggested by *Krasnopolsky* [1986] to case 1, i.e. 70, this would yield a maximum intensity of ~14 kR on Venus in the tropics, which is larger than the maximum intensity of ~5 kR observed on Venus from the Herzberg II band [*Slanger et al.*, 2006]. The laboratory results suggest that the Herzberg I system would be much weaker than the Herzberg II system in a CO_2 atmosphere. Two contributions could explain these discrepancies: extrapolation of the localized intensity maxima on Mars to the Venus atmosphere is not reasonable given the different dynamical processes responsible for the $O(^3P)$ distribution in each atmosphere, or the quenching of $A^3\Sigma_u^+$ is underestimated in our model, indicating that laboratory measurements for collisional removal of $A^3\Sigma_u^+$ are critically needed to properly quantify this emission. Nevertheless, we conclude from this exercise that the quenching rate by CO_2 measured in laboratory for the upper state of the Herzberg I system should be increased by at least one order of magnitude. As for the three-body recombination yield, a relatively small value like the ones used in this study seems to give reasonable emission rates in conjunction with a proper quenching rate. These yields are close to the theoretically calculated ones [*Wraight*, 1982; *Smith*, 1984].

5.2. Herzberg II

[44] The (0-v') progression of the O_2 Herzberg II system is the most intense feature in the visible part of the Venusian spectrum [*Krasnopolsky et al.*, 1976; *Lawrence et al.*, 1977; *Slanger*, 1978; *Kenner et al.*, 1979; *Krasnopolsky and Parshev*, 1983; *Bougher and Borucki*, 1994; *Slanger et al.*, 2001, 2006; *García Muñoz et al.*, 2009], with an average intensity of the total progression of 3–6 kR [*Slanger et al.*, 2008].

[45] Given the fact that we argued previously that case 3 is the optimal set of kinetic parameters to represent the expected emission rate, according to comparison with Venus observations, we suggest that the airglow distribution for the Herzberg II band would resemble that of Figure 7b. The maximum intensity obtained for this case of the Herzberg II simulations is 8 kR before the North Pole winter solstice (L_S = 240–270°) and 5 kR before the South Pole fall equinox (L_S = 150–180°). Globally, the intensity distribution is more pronounced during the polar nights. The emission is weaker between latitudes ±50°, ranging from 20 to 700 R, and in the polar regions during spring and summer.

5.3. Chamberlain

[46] Given the observations of the Chamberlain emission on Venus [*Slanger and Black*, 1978; *Slanger et al.*, 2001; *García Muñoz et al.*, 2009], we expect this emission to occur on Mars as well. However, the intensity of the emission is smaller than that of the Herzberg II band in the Venus atmosphere, according to observations. The ratio of the intensity of the Chamberlain band to that of the Herzberg II band is about 6 according to the discussion of *Slanger et al.* [2001] based on the Venus observations of the Herzberg II band system. Assuming the same chemical mechanism for both Venus and Mars, a rough calculation of the expected intensity of this transition based on the intensity of the Herzberg II band from our simulations gives an expected intensity during the polar nights for the Chamberlain band of as much as 1.3 kR for case 3, and as little as 300 R when considering case 2.

[47] When we use the parameters proposed by *Krasnopolsky* [2011] in our airglow model, i.e. α = 0.12, $k_1 = 2.5{\cdot}3 \times 10^{-33}{\cdot}(300/T)^{3.25}$ cm^6 s^{-1}, $k_O = 1.3 \times 10^{-11}$ cm^3 s^{-1}, and $k_{CO_2} = 4.5 \times 10^{-13}$ cm^3 s^{-1}, we obtain a global distribution of the emission that matches that of the Herzberg I band with slightly larger intensity values (see Figure 7a). This is reasonable since the yield used for the production of the $A'^3\Delta_u$ state is three times larger than that for the $A^3\Sigma_u^-$ state in case 3 of our simulations, while the quenching factor is about 20 times smaller for the Chamberlain band than for the Herzberg I in case 3. The intensity resulting from the Chamberlain transition reaches values above 1 kR after/before the vernal/autumnal equinox and the maximum is found around L_S = 180° in the Southern Hemisphere where the emission is larger than 5 kR. This maximum is greater than expected from the rough calculation inferred from the intensity ratio between the Herzberg II and the Chamberlain observations made in the Venus atmosphere as discussed above.

5.4. IR Atmospheric

5.4.1. 12 LT

[48] The simulations of the variations in latitudes and seasons of the intensity from the IR band at 12 LT give similar results for all cases regarding the structure of the airglow distribution. The major difference between the scenarios simulated here is the range of magnitude of the calculated intensity: case 1 maximum intensity reaches 50 MR, while cases 2 and 3 do not produce intensities exceeding 40 MR, with case 2 producing slightly lower values. Figure 7c shows the global distribution of the daytime IR emission of O_2 following our scenario case 2, which gives smaller intensity maxima, in better agreement with the measurements of the emission on Mars.

[49] The structure of the seasonal and latitudinal distribution of O_2 emissions reflects the ozone distribution and variations. The intensity maxima are located around the polar night terminator on the dayside. The increase in intensity at the terminator encircling the polar winter is a direct consequence of the chemistry that occurs between the

HO_x and O_x species: at high latitudes between 65° to 85° during wintertime, most of the water is condensed on the polar caps which reduce the destruction of O_x through reactions with HO_x [*Lefèvre et al.*, 2004].

[50] We compare our global annual distribution of the daytime IR Atmospheric band for Mars with the Earth ground-based observations made with the IRTF/CSHELL long-slit spectrograph [*Krasnopolsky*, 2003, 2007], the model results of *Krasnopolsky* [2006] and *Krasnopolsky* [2009], and the SPICAM observations [*Fedorova et al.*, 2006a, 2006b]. The structure of the airglow distribution from our simulations is similar to the observations. Overall, our model captures well the seasonal and latitudinal variations of the observed O_2 IR emission. However, coverage of the polar regions, i.e. polarward of ±65°, by observations is sparse.

[51] As for seasonal trends, the intensity increases shortly after winter solstice in the south polar region, i.e. beyond 65°, to reach a maximum intensity above 25 MR around the fall equinox and then decreases until shortly after the summer solstice. Then, the intensity remains low and constant during the polar winter night until it rises before the spring equinox when it reaches another maximum around $L_S = 0°$. In the northern hemisphere, a similar pattern is observed, but here the maximum at $L_S = 0°$ is stronger than at $L_S = 180°$. Moreover, the intensity during the summer season does not reach as low values as in its southern counterpart. Over the equatorial region, the increase in intensity seen in the observations between $L_S = 40–140°$ is also represented in our model.

[52] As per the latitudinal variations of the airglow at different seasons, the trends seen in our model simulations agree well with the available data sets, with case 2 scenario in better agreement for the intensity range. The average intensity between latitudes ±30° varies from 5 to 10 MR for $L_S = 40–140°$ and is below 5 MR for the rest of the year. In the subpolar regions, i.e. between latitudes ±30–65°, all cases seem to overestimate the increase toward the polar terminator. However, *Krasnopolsky* [2003] notes that the airglow intensities observed at these dates for latitudes 50–70°S are unexpectedly low and this could be due to unfavorable observation geometries at the observation dates for the subpolar regions. As for the observations by SPICAM, the coverage was limited in this latitudinal band.

[53] Current nightglow studies favor the use of a relatively high production yield (of 0.7 or larger) for the $a^1\Delta_g$ state in a CO_2 atmosphere [*Crisp et al.*, 1996; *Gérard et al.*, 2008; *Krasnopolsky*, 2011]. Therefore, a quenching rate close to the laboratory upper value of 2×10^{-20} cm^3 s^{-1} [*Sander et al.*, 2006] is needed in order to be in agreement with the current observations of the IR Atmospheric emission on Mars.

5.4.2. 00 LT

[54] OMEGA succeeded in detecting the O_2 IR emission on the nightside of the planet in three limb observations out of 40 [*Bertaux et al.*, 2011, 2012]. The intensity of the measurements is 0.24 MR at $L_S = 120°$ and 76.5°S, 0.15 MR at $L_S = 197°$ and 70°N, and 0.34 MR at $L_S = 3°$ and 85°S [*Bertaux et al.*, 2012].

[55] The intensity of the IR emission at 00 LT resulting from the simulations ranges from 1 to 10 MR, with maxima located at vernal and autumnal equinoxes in each hemisphere. The intensity maxima from case 1 are greater than for cases 2 and 3. Although by comparing our results at 12 LT with SPICAM observations, we would be inclined to favor the parameters used in case 2; for 00 LT, it is more difficult to choose one case over the other. A seasonal map for this emission at 00 LT following the case 2 scenario is shown in Figure 7d. Our model results are in the same range of magnitude as the values from OMEGA.

[56] Table 1 reports on the individual measurements of the nighttime O_2 1.27-μm emission made with OMEGA [*Bertaux et al.*, 2012] and also with SPICAM [*Fedorova et al.*, 2012] along with our model results for the same location and season. To reduce the effect of local dynamical variations in the atmosphere, we also computed the average of the intensity over 10° of L_S centered around the season of the observation. We notice from this table that in most instances, the modeled intensity is smaller than the measured intensity. Also, the values are generally closer to the observed vertically integrated intensity for the period $L_S = 111–120°$, while for the period $L_S = 152–164°$, the model clearly underestimates the measured intensities. For the peak altitude, our model is in good agreement with the SPICAM's derived altitudes of the maxima, while it overestimates the altitude as compared to the OMEGA results. In general, we are satisfied with the realistic representation of the measurements from the simulations with our airglow model. We advise the reader to take into consideration that our model is used for a climatological study of the airglow distribution, while the observations represent single-point measurements that are subject to short time-scale variations due to the, e.g. solar activity, meteorological conditions, etc. We therefore do not expect a perfect match between the model results and the measurements.

[57] From our simulations, we observe day-to-night variations over the polar regions that do not exceed more than one order of magnitude difference for all cases. This is a consequence of the constant solar illumination at high latitudes in summertime. In the regions of permanent day, i.e. summer poles, the O_2 emission includes a contribution from O_3 photolysis, which is visible in Figure 7c for the Northern Hemisphere. By contrast, in the latitudinal band ±50°, the intensity ranges from 1 to 100 kR at 00 LT, much weaker than the simulated intensities at 12 LT (0.5–2 MR). This temporal variation is a consequence of the increased production of $a^1\Delta_g$ at 12 LT from the photolysis of O_3.

6. Sensitivity to Dust and Water Levels

[58] Dust and water can vary strongly in the Mars atmosphere. As shown by the continuous measurements of temperature, dust, and water from the Mars Climate Sounder on MRO [*McCleese et al.*, 2010], the main effect of dust is to warm the atmosphere, allowing more H_2O to be transported upwards. This is the reason O_3 disappears almost completely during the perihelion season, and hence the O_2 emission caused by photolysis also vanishes [*Lefèvre et al.*, 2004]. The effect of dust on photolysis rates is therefore expected to be negligible compared to the change in H_2O that occurs at the same time.

[59] As mentioned above, simulations of the O_2 airglow emissions for the IR Atmospheric emission were performed with three different runs of the LMD-MGCM. The goal of this exercise is to study the response of the airglow

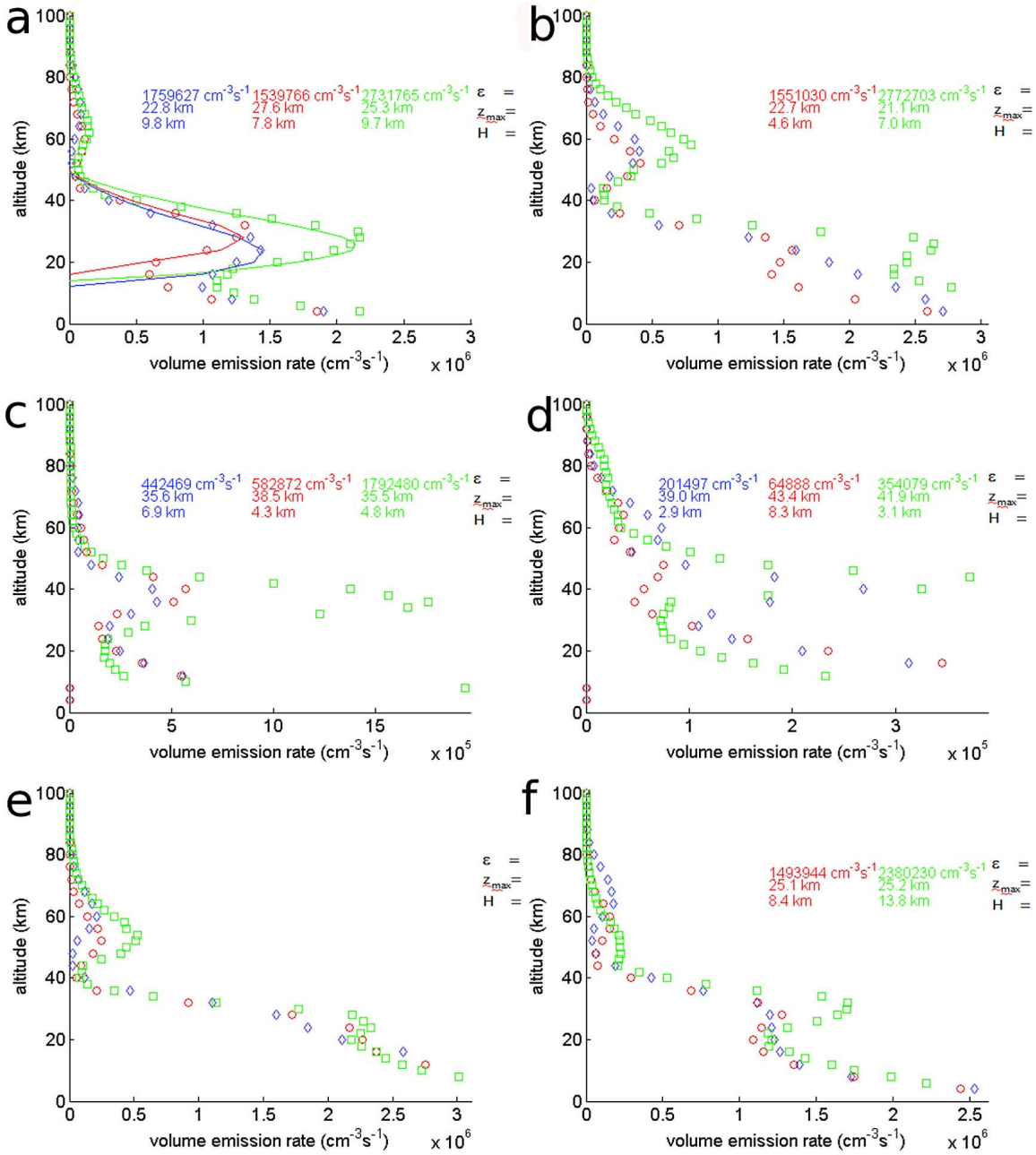

Figure 8. VER profiles for the O_2 IR Atmospheric emission at 12 LT at (left) $L_S = 0°$ and (right) $L_S = 180°$ for latitudes (top) 67.5°N, (middle) 0°, and (bottom) 67.5°S for three GCM data sets called "runs" and the case 2 of kinetic parameters sets (see text for details). Blue features are used for run 1, red for run 2, and green for run 3. The symbols are the calculated VER at each altitude from the airglow model, while the line corresponds to the Chapman layer fit for each VER profile; the fitting parameters, ϵ_{max} (Figure 8, top), z_{max} (Figure 8, middle), and H (Figure 8, bottom), are given.

emissions to changes in the dust and water load. It is obvious from Figures 1 and 2 that differences in the dust and water schemes induce variations in the temperature, atomic oxygen density, and ozone density profiles. The CO_2 profile is however negligibly affected. The temperature vertical distribution of temperature shows greater variations between run 1 and run 2, than between run 2 and run 3, indicating that changes in the dust level have the greater impact on the temperature profile. As for the atomic oxygen and ozone density distributions, the vertical structure is more similar between runs 1 and 2 as compared to run 3, meaning that the water cycle has a stronger effect on the oxygen chemistry than the dust level. These behaviors are not surprising since current observations revealed similar trends [e.g., *McCleese et al.*, 2010].

[60] Given the impact of the water and dust content on the atmospheric composition and temperature structure, we would expect to see variations in the vertical structure of the

airglow emissions. As for the VER profiles, shown in Figure 8, there is more similarity between the profiles performed with runs 1 and 2 above 50 km in altitude at latitude ±67.5°. Above this altitude, the emission rate from run 3 is typically stronger and peaks at lower altitudes than for the two other runs. This pattern illustrates the impact of the water cycle on the oxygen chemistry, which directly affects the emission profile. Below 50 km, the profiles from runs 2 and 3 have a similar structure, although the emission rate from run 3 is greater than for run 2; the profile from run 1 does not follow the structure of the two other cases. This behavior would be due to changes in dust levels affecting mostly the lower atmosphere.

[61] Over the equator, the emission rate from run 3 is much larger than for the two other cases above 30 km. The profiles from runs 1 and 2 have a similar behavior below 30 km, as compared to that from run 3. Dust load would be responsible for the observed difference: dust has a strong impact on daytime surface heating such that the more photons with short wavelengths, i.e. wavelengths in the UV range, reaching the lower atmosphere, the more atomic oxygen is produced due to ozone photodissociation. In contrast, the water cycle has a direct impact on the oxygen species, particularly over the polar regions where most of the cycling between the HO_x radicals and reservoir species come into play [*Lefèvre et al.*, 2004]. We would expect very subtle variations from the dust cycle beyond the subtropics because of the longer mean free path that reduces the solar flux at the surface.

7. Summary

[62] In this paper, we have investigated the global distribution of the emission profile and integrated intensity of four emissions of O_2 airglow in a CO_2 atmosphere: the Herzberg I and II, the Chamberlain, and the IR Atmospheric occurring from the UV to the IR spectral region. Although none of the O_2 visible emissions have been observed on Mars at night, most probably because of the inadequate signal-to-noise ratio of the previous instruments, the observations of the Herzberg II and Chamberlain band systems in the Venus atmosphere motivate this study. Our simulations agree with the previous works done on suggestions that the Herzberg II band emission is the most promising candidate for a successful detection in the visible spectral range [*Mullen et al.*, 2006; *Krasnopolsky*, 2011].

[63] Strong latitudinal and seasonal differences in the O_2 airglow emissions were highlighted in this work, with stronger emissions occurring at the poles along the terminator. Another feature of our model simulations is the frequent occurrence of structures in the vertical distribution of the emissions studied here. On Earth, frequent occurrences of double-layer structures in airglow have been reported by *Melo et al.* [2000] and further studied in models. Double-peaked vertical profiles of airglow emissions have been observed on Mars by CRISM [*Clancy et al.*, 2011; Clancy et al., submitted, 2012] and on Venus by VIRTIS [*Piccioni et al.*, 2009]. This model study strengthens the argument for using 3-D models to provide dynamical variations for representing realistic simulations of the vertical structure and global distribution of airglow features.

[64] As expected, the molecular oxygen emissions are directly affected by variations in the vertical structure of the temperature and O_x species concentration. Our sensitivity study shows the response of the airglow emissions to different levels of water and dust content. The airglow layer at low altitudes, a typical feature of daytime equatorial emissions, responds directly to variations in dust levels, while the emissions observed during the polar nights are modulated by the water distribution, which is anti-correlated with the ozone concentration. Thus, airglow provides a useful tool for characterizing the actual state of the atmosphere.

[65] To improve Martian airglow modeling, and therefore to improve the reliability of using airglow as a proxy for atomic oxygen density and temperature profiles, laboratory measurements are required to quantify the kinetics of the reaction chain that produce the O_2 airglow. Alternatively, an instrument that could measure the VER of these emissions simultaneously with some precision, i.e. within an error margin of 10%, could allow for a clear identification of the physical chemistry processes. In particular, knowledge of the quenching rates of the excited states by CO_2 is needed. Further, we need a better description of the recombination reaction of O in a CO_2 atmosphere at low temperatures and the determination of the pathways from collisional removal of the excited O_2 molecules with CO_2 and CO.

[66] Much information has been gained about oxygen photochemistry in a CO_2 dominated atmosphere by the availability of airglow measurements for both Mars and Venus. We believe that more precision on the intensity and VER estimates can be gained by absolute calibrated measurements of oxygen airglow covering both the visible and IR spectral regions on Mars and Venus for nighttime conditions. Finally, the work presented here provides a first step in our efforts to design an instrument for the detection of airglow emission for atomic oxygen density and temperature sounding in the Mars atmosphere to improve the required knowledge of the atmosphere in support of the safe landing of future missions on the planet's surface.

[67] **Acknowledgments.** The authors are very grateful to Tom G. Slanger for his feedback on the preliminary versions of this manuscript. M.-E. Gagné would like to acknowledge the Fonds Québécois de la Recherche sur la Nature et les Technologies, the Natural Sciences and Engineering Research Council of Canada, and the Canadian Space Agency for supporting this research. F. González-Galindo has been partially funded by a CSIC JAE-Doc contract co-financed by the European Social Fund.

References

Angelats i Coll, M., F. Forget, M. A. López-Valverde, and F. González-Galindo (2005), The first Mars thermospheric general circulation model: The Martian atmosphere from the ground to 240 km, *Geophys. Res. Lett.*, *32*, L04201, doi:10.1029/2004GL021368.

Barth, C. A., C. W. Hord, J. B. Pearce, K. K. Kelly, G. P. Anderson, and A. I. Stewart (1971), Mariner-6 and Mariner-7 Ultraviolet spectrometer experiment: Upper atmosphere data, *J. Geophys. Res.*, *76*(10), 2213–2227, doi:10.1029/JA076i010p02213.

Barth, C. A., A. L. Lane, A. I. Stewart, and C. W. Hord (1972), Mariner-9 Ultraviolet experiment: Mars airglow spectroscopy and variations in Lyman alpha, *Icarus*, *17*(2), 457–468.

Bates, D. R. (1988), Excitation and quenching of the oxygen bands in the nightglow. *Planet. Space Sci.*, *36*(9), 875–881.

Bates, D. R. (1989), Oxygen band system transition arrays, *Planet. Space Sci.*, *37*(7), 881–887.

Baulch, D. L., D. D. Drysdale, J. Duxbury, and S. J. Grant (1976), *Evaluated Kinetic Data for High Temperature Reactions*, vol. 3, *Homogeneous*

Gas Phase Reactions of the O_2-O_3 System, the CO-O_2-H_2 System, and of Sulfur-Containing Species, technical report, Butterworth, London.

Bertaux, J. L., et al. (2006), SPICAM on Mars Express: Observing modes and overview of UV spectrometer data and scientific results, *J. Geophys. Res.*, *111*, E10S90, doi:10.1029/2006JE002690.

Bertaux, J.-L., B. Gondet, J. P. Bibring, F. Montmessin, and F. Lefèvre (2011), First detection of O_2 recombination nightglow emission at 1.27 μm in the atmosphere of Mars with OMEGA/MEX and comparison with model, paper presented at the Fourth International Mars Atmosphere Workshop: Modelling and Observations, CNES, Paris, 8–11 February.

Bertaux, J.-L., B. Gondet, J. Bibring, F. Montmessin, and F. Lefèvre (2012), First detection of O_2 1.27-μm nightglow emission at Mars with OMEGA/MEX and comparison with general circulation model predictions, *J. Geophys. Res.*, *117*, E00J04, doi:10.1029/2011JE003890.

Bougher, S. W., and W. J. Borucki (1994), Venus O_2 visible and IR nightglow: Implications for lower thermosphere dynamics and chemistry. *J. Geophys. Res.*, *99*(E2), 3759–3776.

Bougher, S. W., S. Engel, R. G. Roble, and B. Foster (1999), Comparative terrestrial planet thermospheres: 2. Solar cycle variation of global structure and winds at equinox, *J. Geophys. Res.*, *104*(E7), 16,591–16,611.

Bougher, S. W., S. Rafkin, and P. Drossart (2006), Dynamics of the Venus upper atmosphere: Outstanding problems and new constraints expected from Venus Express, *Planet. Space Sci.*, *54*(13–14), 1371–1380.

Campbell, I. M., and C. N. Gray (1973), Rate constants for O(^{3}P) recombination and association with N(^{4}S), *Chem. Phys. Lett.*, *18*(4), 607–609.

Campbell, I. M., and B. A. Thrush (1967), Recombination of nitrogen atoms and the nitrogen afterglow, *Proc. R. Soc. London Ser. A*, *296*(1445), 201–221.

Clancy, R. T., B. J. Sandor, M. J. Wolff, P. R. Christensen, M. D. Smith, J. C. Pearl, B. J. Conrath, and R. J. Wilson (2000), An intercomparison of ground-based millimeter, MGS TES, and Viking atmospheric temperature measurements: Seasonal and interannual variability of temperatures and dust loading in the global Mars atmosphere, *J. Geophys. Res.*, *105*(E4), 9553–9571.

Clancy, R. T., M. Wolff, M. Smith, B. Cantor, and F. Lefèvre (2011), MRO CRISM and MARCI observations of Mars ozone, paper presented at the Fourth International Mars Atmosphere Workshop: Modelling and Observations, CNES, Paris, 8–11 February.

Copeland, R. A. (1994), Laser double-resonance study of the collisional removal of $O_2(A^3\Sigma_u^+, v = 7)$ with O_2, *J. Chem. Phys.*, *100*(1), 744–745.

Copeland, R. A., K. Knutsen, M. E. Onishi, and T. Yalcin (1996), Collisional removal of $O_2(c^1\Sigma_u^-, v = 9)$ by O_2, N_2, and He, *J. Chem. Phys.*, *105*(23), 10,349–10,355.

Cox, C., A. Saglam, J. C. Gérard, J. L. Bertaux, F. González-Galindo, F. Leblanc, and A. Reberac (2008), Distribution of the ultraviolet nitric oxide Martian night airglow: Observations from Mars Express and comparisons with a one-dimensional model, *J. Geophys. Res.*, *113*, E08012, doi:10.1029/2007JE003037.

Cox, C., J.-C. Gérard, B. Hubert, J.-L. Bertaux, and S. W. Bougher (2010), Mars ultraviolet dayglow variability: SPICAM observations and comparison with airglow model, *J. Geophys. Res.*, *115*, E04010, doi:10.1029/2009JE003504.

Crisp, D., V. S. Meadows, B. Bézard, C. deBergh, J. P. Maillard, and F. P. Mills (1996), Ground-based near-infrared observations of the Venus nightside: 1.27-μm $O_2(a^1\Delta_g)$ airglow from the upper atmosphere, *J. Geophys. Res.*, *101*(E2), 4577–4593.

Farrel, A., T. Dunne, R. Novak, Y. Cabral, M. J. Mumma, and B. Bonev (2005), Seasonal mapping of ozone in the middle atmosphere of Mars, *Bull. Am. Astron. Soc.*, *36*, 1158.

Fedorova, A. A., O. I. Korablev, S. Perrier, J.-L. Bertaux, F. Lefèvre, and A. Rodin (2006a), Observation of O_2 1.27 μm dayglow by SPICAM IR: Seasonal distribution for the first Martian year of Mars Express, *J. Geophys. Res.*, *111*, E09S07, doi:10.1029/2006JE002694.

Fedorova, A. A., O. I. Korablev, S. Perrier, J. L. Bertaux, F. Lefèvre, A. Rodin, and A. Kiselev (2006b), Exploration of Mars in the SPICAM-IR experiment onboard the Mars-Express spacecraft: 2. Nadir observations: Simultaneous observations of water vapor and O_2 glow in the Martian atmosphere, *Cosmic Res.*, *44*(4), 294–304.

Fedorova, A. A., S. Guslyakova, F. Lefèvre, J.-L. Bertaux, O. Korablev, F. Montmessin, A. Reberac, and B. Gondet (2012), The O_2 nightglow in the Martian atmosphere by SPICAM onboard of Mars-Express, *Icarus*, *219*, 596–608.

Forget, F., F. Hourdin, R. Fournier, C. Hourdin, O. Talagrand, M. Collins, S. R. Lewis, P. L. Read, and J. P. Huot (1999), Improved general circulation models of the Martian atmosphere from the surface to above 80 km, *J. Geophys. Res.*, *104*(E10), 24,155–24,175.

Forget, F., F. Montmessin, J. L. Bertaux, F. González-Galindo, B. Lebonnois, E. Quémerais, A. Reberac, E. Dimarellis, and M. A. López-Valverde (2009), Density and temperatures of the upper Martian atmosphere measured by stellar occultations with Mars Express SPICAM, *J. Geophys. Res.*, *114*, E01004, doi:10.1029/2008JE003086.

García Muñoz, A., F. P. Mills, T. G. Slanger, G. Piccioni, and P. Drossart (2009), Visible and near-infrared nightglow of molecular oxygen in the atmosphere of Venus, *J. Geophys. Res.*, *114*, E12002, doi:10.1029/2009JE003447.

Gérard, J. C., A. Saglam, G. Piccioni, P. Drossart, C. Cox, S. Erard, R. Hueso, and A. Sanchez-Lavega (2008), Distribution of the O_2 infrared nightglow observed with VIRTIS on board Venus Express, *Geophys. Res. Lett.*, *35*, L02207, doi:10.1029/2007GL032021.

Gondet, B., J.-P. Bibring, J.-L. Bertaux, and F. Montmessin (2010), O_2 nightglow emission detection in the atmosphere of Mars, identified by the OMEGA/MEx investigation, paper presented at EGU General Assembly 2010, BM.W_F, Vienna, 2–7 May.

González-Galindo, F., M. A. López-Valverde, M. Angelats i Coll, and F. Forget (2005), Extension of a Martian general circulation model to thermospheric altitudes: UV heating and photochemical models, *J. Geophys. Res.*, *110*, E09008, doi:10.1029/2004JE002312.

González-Galindo, F., G. Gilli, M. A. López-Valverde, F. Forget, and F. Leblanc (2008), Nitrogen and ionospheric chemistry in the thermospheric LMD-MGCM, paper presented at Third International Workshop on The Mars Atmosphere: Modelling and Observations, Lunar and Planet. Inst., Williamsburg, Va, 10–13 November.

González-Galindo, F., F. Forget, M. A. López-Valverde, M. Angelats i Coll, and E. Millour (2009), A ground-to-exosphere Martian general circulation model: 1. Seasonal, diurnal, and solar cycle variation of thermospheric temperatures, *J. Geophys. Res.*, *114*, E04001, doi:10.1029/2008JE003246.

Huestis, D. L., R. A. Copeland, K. Knutsen, T. G. Slanger, R. T. Jongma, M. G. H. Boogaarts, and G. Meijer (1994), Branch intensities and oscillator-strengths for the Herzberg absorption systems in oxygen, *Can. J. Phys.*, *72*(11–12), 1109–1121.

Huestis, D. L., S. W. Bougher, J. L. Fox, M. Galand, R. E. Johnson, J. I. Moses, and J. C. Pickering (2008), Cross sections and reaction rates for comparative planetary aeronomy, *Space Sci. Rev.*, *139*(1–4), 63–105.

Hwang, E. S., and R. A. Copeland (1997), Temperature dependence of the collisional removal of $O_2(A^3\Sigma_u^+, v = 9)$ with O_2 and N_2, *Geophys. Res. Lett.*, *24*(6), 643–646.

Jamieson, C. S., R. M. García, C. S. Jamieson, D. Pejaković, and K. Kalogerakis (2009), The kinetics of oxygen atom recombination in the presence of carbon dioxide, *EOS Trans. AGU*, *90*(52), Fall Meet. Suppl., Abstract P51D-1156.

Kenner, R. D., and E. A. Ogryzlo (1980), Deactivation of $O_2(A^3\Sigma_u^+)$ by O_2, O, and Ar, *Int. J. Chem. Kinetics*, *12*(7), 501–508.

Kenner, R. D., and E. A. Ogryzlo (1983a), Quenching of $O_2(c^1\Sigma_u^-, v = 0)$ by O(^{3}P), $O_2(A^1\Delta_g)$, and other gases, *Can. J. Chem.*, *61*(5), 921–926.

Kenner, R. D., and E. A. Ogryzlo (1983b), Rate constant for the deactivation of $O_2(A^3\Sigma_u^+)$ by N_2, *Chem. Phys. Lett.*, *103*(3), 209–212.

Kenner, R. D., and E. A. Ogryzlo (1984), Quenching of the O_2(A, v = 2-X, v = 5) Herzberg-I band by O_2(A) and O, *Can. J. Phys.*, *6*(212), 1599–1602.

Kenner, R. D., E. A. Ogryzlo, and S. Turley (1979), Excitation of the night airglow of Earth, Venus and Mars, *J. Photochem.*, *10*(2), 199–204.

Knutsen, K., M. J. Dyer, and R. A. Copeland (1994), Laser double-resonance study of the collisional removal of $O_2(A^3\Sigma_u^+)$ v = 6, 7, and 9 with O_2, N_2, CO_2, Ar and He, *J. Chem. Phys.*, *101*(9), 7415–7422.

Krasnopolsky, V. A. (1981), Excitation of oxygen emissions in the night airglow of the terrestrial planets, *Planet. Space Sci.*, *29*(9), 925–929.

Krasnopolsky, V. A. (1986), Oxygen emissions in the night airglow of the Earth, Venus and Mars, *Planetary and Space Science*, *34*(6), 511–518.

Krasnopolsky, V. A. (1995), Uniqueness of a solution of a steady-state photochemical problem - Applications to Mars, *J. Geophys. Res.*, *100*(E2), 3263–3276.

Krasnopolsky, V. A. (2003), Mapping of Mars O_2 1.27-μm dayglow at four seasonal points, *Icarus*, *165*(2), 315–325.

Krasnopolsky, V. A. (2006), Photochemistry of the Martian atmosphere: Seasonal, latitudinal, and diurnal variations, *Icarus*, *185*(1), 153–170.

Krasnopolsky, V. A. (2007), Long-term spectroscopic observations of Mars using IRTF/CSHELL: Mapping of O_2 dayglow, CO, and search for CH_4, *Icarus*, *190*(1), 93–102.

Krasnopolsky, V. A. (2009), Seasonal variations of photochemical tracers at low and middle latitudes on Mars: Observations and models, *Icarus*, *201*(2), 564–569.

Krasnopolsky, V. A. (2010), Venus night airglow: Ground-based detection of OH, observations of O_2 emissions, and photochemical model, *Icarus*, *207*(1), 17–27.

Krasnopolsky, V. A. (2011), Excitation of the oxygen nightglow on the terrestrial planets, *Planet. Space Sci.*, *59*(8), 754–766, doi:10.1016/j.pss.2011.02.015.

Krasnopolsky, V. A., and G. L. Bjoraker (2000), Mapping of Mars $O_2(^1\Delta)$ dayglow, *J. Geophys. Res.*, *105*(E8), 20,179–20,188.

Krasnopolsky, V. A., and A. A. Krysko (1976), On the night airglow of the Martian atmosphere, *Space Res.*, *16*, 1005–1008.

Krasnopolsky, V. A., and V. A. Parshev (1983), *Photochemistry of the Venus Atmosphere*, Univ. of Ariz. Press, Tucson.

Krasnopolsky, V. A., and G. V. Tomashova (1980), Venus nightglow variations, *Space Res.*, Preprint 552, Space Res. Inst., Moscow.

Krasnopolsky, V. A., A. A. Krysko, V. N. Rogachev, and V. A. Parshev (1976), The spectrum of the Venus night airglow: Identification problem, *Space Res.*, Preprint 244, Space Res. Inst., Moscow.

Lafferty, W. J., A. M. Solodov, C. L. Lugez, and G. T. Fraser (1998), Rotational line strengths and self-pressure-broadening coefficients for the 1.27-μm, $a^1\Delta_g - X^3\Sigma_g^-$, v = 0-0 band of O_2, *Appl. Opt.*, *37*(12), 2264–2270.

Lawrence, G. M., C. A. Barth, and V. Argabright (1977), Excitation of Venus night airglow, *Science*, *195*(4278), 573–574.

Lefèvre, F., S. Lebonnois, F. Montmessin, and F. Forget (2004), Three-dimensional modeling of ozone on Mars, *J. Geophys. Res.*, *109*, E07004, doi:10.1029/2004JE002268.

Lefèvre, F., J. L. Bertaux, R. T. Clancy, T. Encrenaz, K. Fast, F. Forget, S. Lebonnois, F. Montmessin, and S. Perrier (2008), Heterogeneous chemistry in the atmosphere of Mars, *Nature*, *454*(7207), 971–975.

López-Puertas, M., and M. A. López-Valverde (1995), Radiative energy-balance of CO_2 non-LTE infrared emissions in the Martian atmosphere, *Icarus*, *114*(1), 113–129.

McCleese, D., and D. M. Kass (2010), Results of the Mars climate investigations on the Mars Reconnaissance Orbiter, Abstract C31-0014-10 presented at the 38th COSPAR Scientific Assembly 2010, COSPAR, Bremen, Germany, 18–25 July.

McCleese, D. J., et al. (2010), Structure and dynamics of the Martian lower and middle atmosphere as observed by the Mars Climate Sounder: Seasonal variations in zonal mean temperature, dust, and water ice aerosols, *J. Geophys. Res.*, *115*, E12016, doi:10.1029/2010JE003677.

McDunn, T. L., S. W. Bougher, J. Murphy, M. D. Smith, F. Forget, J.-L. Bertaux, and F. Montmessin (2010), Simulating the density and thermal structure of the middle atmosphere (~80–130 km) of Mars using the MGCM-MTGCM: A comparison with MEX/SPICAM observations, *Icarus*, *206*(1), 5–17.

Melo, S. M. L., R. P. Lowe, and J. P. Russell (2000), Double-peaked hydroxyl airglow profiles observed from WINDII/UARS, *J. Geophys. Res.*, *105*(D10), 12,397–12,403.

Melo, S. M. L., I. C. McDade, and H. Takahashi (2001), Atomic oxygen density profiles from ground-based nightglow measurements at 23 degrees S, *J. Geophys. Res.*, *106*(D14), 15,377–15,384.

Migliorini, A., et al. (2011), Oxygen airglow emission on Venus and Mars as seen by VIRTIS/VEX and OMEGA/MEX imaging spectrometers, *Planet. Space Sci.*, *59*(10), 981–987.

Montmessin, F., F. Forget, P. Rannou, M. Cabane, and R. M. Haberle (2004), Origin and role of water ice clouds in the Martian water cycle as inferred from a general circulation model, *J. Geophys. Res.*, *109*, E10004, doi:10.1029/2004JE002284.

Mullen, C., E. Bolin, R. A. Copeland, and T. G. Slanger (2006), Collisional removal of highly vibrational excited oxygen in the c state, *EOS Trans. AGU*, *87*(52), Fall Meet. Suppl., Abstract SA33A-0253.

Nair, H., M. Allen, A. D. Anbar, Y. L. Yung, and R. T. Clancy (1994), A photochemical model of the Martian atmosphere, *Icarus*, *111*(1), 124–150.

Newman, S. M., I. C. Lane, A. J. Orr-Ewing, D. A. Newnham, and J. Ballard (1999), Integrated absorption intensity and Einstein coefficients for the O_2 $a^1\Delta_g - X^3\Sigma_g^-$ (0, 0) transition: A comparison of cavity ringdown and high resolution Fourier transform spectroscopy with a long-path absorption cell, *J. Chem. Phys.*, *110*(22), 10,749–10,757.

Novak, R. E., M. J. Mumma, M. A. DiSanti, N. Dello Russo, and K. Magee-Sauer (2002), Mapping of ozone and water in the atmosphere of Mars near the 1997 aphelion, *Icarus*, *158*(1), 14–23.

Novak, R. E., M. J. Mumma, S. Lee, L. Ivanov, B. Bonev, and G. Villanueva (2005), Mapping of D/H ratio in the Martian atmosphere near the perihelion, *Bull. Am. Astron. Soc.*, *37*, 669.

Noxon, J. F., W. A. Traub, N. P. Carleton, and P. Connes (1976), Detection of O_2 dayglow emissions from Mars and Martian ozone abundance, *Astrophys. J.*, *207*(3), 1025–1035.

Pejaković, D. A., K. S. Kalogerakis, R. A. Copeland, and D. L. Huestis (2008), Laboratory determination of the rate coefficient for three-body recombination of oxygen atoms in nitrogen, *J. Geophys. Res.*, *113*, A04303, doi:10.1029/2007JA012694.

Piccioni, G., L. Zasova, A. Migliorini, P. Drossart, A. Shakun, A. G. Muñoz, F. P. Mills, and A. Cardesin-Moinelo (2009), Near-IR oxygen nightglow observed by VIRTIS in the Venus upper atmosphere, *J. Geophys. Res.*, *114*, E00B38, doi:10.1029/2008JE003133.

Royer, E., F. Montmessin, and J.-L. Bertaux (2010), NO emissions as observed by SPICAV during stellar occultations, *Planet. Space Sci.*, *58*(10), 1314–1326.

Sander, S. P., et al. (2006), Chemical kinetics and photochemical data for use in atmospheric studies, *JPL Publ. 06-2, Tech. Rep. 15*, Jet Propul. Lab., Pasadena, Calif.

Sharp, W. E., and I. C. McDade (1996), Peak height and density of the mesospheric oxygen layer from ground based airglow measurements, *EOS Trans. AGU*, *77*(46), Fall Meet. Suppl., Abstract F547.

She, C. Y., and R. P. Lowe (1998), Seasonal temperature variations in the mesopause region at mid-latitude: comparison of lidar and hydroxyl rotational temperatures using WINDII/UARS OH height profiles, *J. Atmos. Sol. Terr. Phys.*, *60*(16), 1573–1583.

Slanger, T. G. (1978), Generation of $O_2(c^1\Sigma_u^-, C^3\Delta_u, A^3\Sigma_u^+)$ from oxygen atom recombination, *J. Chem. Phys.*, *69*(11), 4779–4791.

Slanger, T. G., and G. Black (1978), $O_2(C^3\Delta_u \rightarrow a^1\Delta_g)$ bands in nightglow spectrum of Venus, *Geophys. Res. Lett.*, *5*(11), 947–948.

Slanger, T. G., and R. A. Copeland (2003), Energetic oxygen in the upper atmosphere and the laboratory, *Chem. Rev.*, *103*(12), 4731–4765.

Slanger, T. G., P. C. Cosby, D. L. Huestis, and T. A. Bida (2001), Discovery of the atomic oxygen green line in the Venus night airglow, *Science*, *291*(5503), 463–465.

Slanger, T. G., D. L. Huestis, P. C. Cosby, N. J. Chanover, and T. A. Bida (2006), The Venus nightglow: Ground-based observations and chemical mechanisms, *Icarus*, *182*(1), 1–9.

Slanger, T. G., C. Mullen, E. Bolin, and R. A. Copeland (2007), Venus photochemistry and ground-based observations, Abstract 9007 presented at the Workshop on Planetary Atmospheres, NASA Goddard Space Flight Cent., Greenbelt, Md, 6–7 November.

Slanger, T. G., T. E. Cravens, J. Crovisier, S. Miller, and D. F. Strobel (2008), Photoemission phenomena in the solar system, *Space Sci. Rev.*, *139*, 267–310.

Smith, G. P., and R. Robertson (2008), Temperature dependence of oxygen atom recombination in nitrogen after ozone photolysis, *Chem. Phys. Lett.*, *458*(1–3), 6–10.

Smith, I. W. M. (1984), The role of electronically excited-states in recombination reactions, *Int. J. Chem. Kinetics*, *16*(4), 423–443.

Steadman, J. A., and B. A. Thrush (1994), A laboratory study of the mechanism of the oxygen airglow, *J. Atmos. Chem.*, *18*(4), 301–317.

Stott, I. P., and B. A. Thrush (1989), Laboratory studies of the mechanism of the oxygen nightglow, *Proc. R. Soc. London Ser. A*, *424*(1866), 1–17.

Traub, W. A., N. P. Carleton, P. Connes, and J. F. Noxon (1979), Latitude variation of O_2 dayglow and O_3 abundance on Mars, *Astrophys. J.*, *229*(2), 846–850.

Wraight, P. C. (1982), Association of atomic oxygen and airglow excitation mechanisms. *Planet. Space Sci.*, *30*(3), 251–259.